

Avoided metallicity in a hole-doped Mott insulator on a triangular lattice

Received: 13 January 2024

Accepted: 21 August 2024

Published online: 16 September 2024

Check for updates

Chi Ming Yim ^{1,2,8} ✉, Gesa-R. Siemann ^{1,8}, Srdjan Stavrčić ^{3,4,8},
Seunghyun Khim ⁵, Izidor Benedičič ¹, Philip A. E. Murgatroyd¹,
Tommaso Antonelli¹, Matthew D. Watson ⁶, Andrew P. Mackenzie ^{1,5},
Silvia Picozzi³ ✉, Phil D. C. King ¹ ✉ & Peter Wahl ^{1,7} ✉

Doping of a Mott insulator gives rise to a wide variety of exotic emergent states, from high-temperature superconductivity to charge, spin, and orbital orders. The physics underpinning their evolution is, however, poorly understood. A major challenge is the chemical complexity associated with traditional routes to doping. Here, we study the Mott insulating CrO_2 layer of the delafossite PdCrO_2 , where an intrinsic polar catastrophe provides a clean route to doping of the surface. From scanning tunnelling microscopy and angle-resolved photoemission, we find that the surface stays insulating accompanied by a short-range ordered state. From density functional theory, we demonstrate how the formation of charge disproportionation results in an insulating ground state of the surface that is disparate from the hidden Mott insulator in the bulk. We demonstrate that voltage pulses induce local modifications to this state which relax over tens of minutes, pointing to a glassy nature of the charge order.

The Mott–Hubbard Hamiltonian is one of the simplest models to describe correlated electron physics, capturing phenomena ranging from antiferromagnetic order in a Mott insulator to potentially explaining the high-temperature superconductivity in cuprates. It yields particularly exciting predictions for systems on triangular lattices, including, for a single-orbital Hubbard model, the famed resonating valence bond state¹, and the formation of quantum spin liquids and complex magnetic orders². In multi-orbital systems, the situation is even richer: for example, for transition metal atoms with a partially filled t_{2g} manifold, the interplay of spin–orbit coupling with correlations can result in topologically non-trivial fractional Chern states^{3,4}, while charge carrier doping can lead to exotic superconducting states⁵. This large variety of unconventional ground states motivates the study

of triangular-lattice Mott systems experimentally, and in particular probing the evolution of their ground states with doping.

Here, we establish the surface of PdCrO_2 as a model system in which to investigate the competing ground states of a doped triangular-lattice Mott system. Its bulk crystal structure (Fig. 1a) consists of stacked triangular-lattice Pd^{1+} and $(\text{CrO}_2)^{-}$ layers. The former is in a $4d^9$ charge state, forming highly conductive metallic layers^{6–9}. In contrast, the latter host Cr^{3+} ions, with a $3d^3$ electron configuration which half-fills the t_{2g} manifold. These layers are Mott insulating, and develop an $S = 3/2$ antiferromagnetic (AF) order below a Néel temperature of $T_N = 37.5 \text{ K}$ ^{8,10–12}. This naturally occurring heterostructure of metallic and Mott-insulating layers makes this “hidden” Mott state¹² an ideal candidate for detailed spectroscopic study⁸.

¹SUPA, School of Physics and Astronomy, University of St Andrews, North Haugh, St Andrews, Fife KY16 9SS, UK. ²Tsung Dao Lee Institute and School of Physics and Astronomy, Shanghai Jiao Tong University, 201210 Shanghai, China. ³Consiglio Nazionale delle Ricerche (CNR-SPIN), Unità di Ricerca presso Terzi c/o Università “G. D’Annunzio”, 66100 Chieti, Italy. ⁴Vinča Institute of Nuclear Sciences -National Institute of the Republic of Serbia, University of Belgrade, P. O. Box 522, RS-11001 Belgrade, Serbia. ⁵Max Planck Institute for Chemical Physics of Solids, Nöthnitzer Straße 40, 01187 Dresden, Germany. ⁶Diamond Light Source, Harwell Science and Innovation Campus, Didcot OX11 0DE, UK. ⁷Physikalisches Institut, Universität Bonn, Nussallee 12, 53115 Bonn, Germany. ⁸These authors contributed equally: Chi Ming Yim, Gesa-R. Siemann, Srdjan Stavrčić. ✉ e-mail: c.m.yim@sjtu.edu.cn; silvia.picozzi@spin.cnr.it; pdk6@st-andrews.ac.uk; wahl@st-andrews.ac.uk

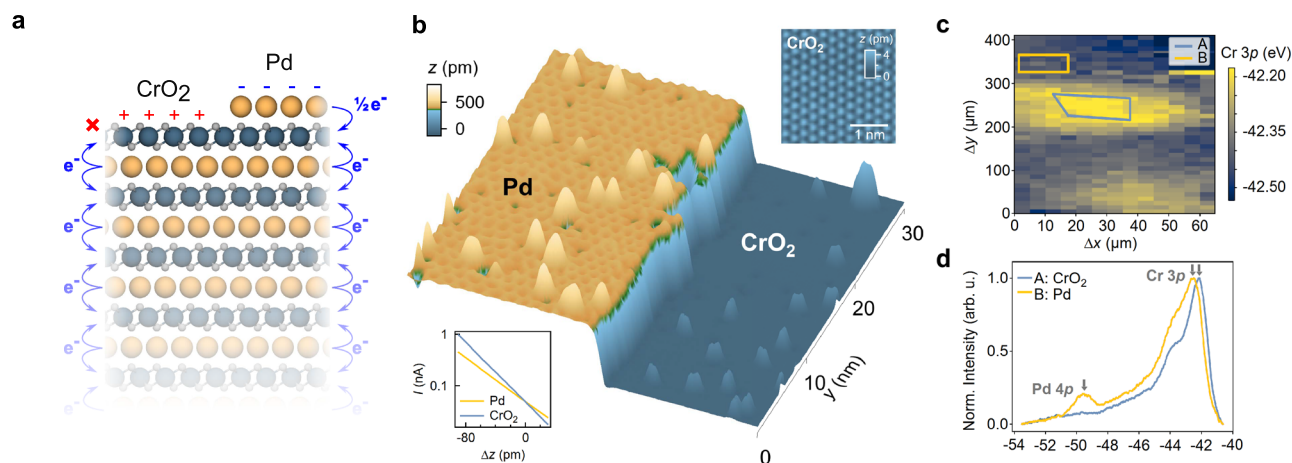


Fig. 1 | Surface terminations of the delafossite PdCrO₂. **a** Crystal structure of PdCrO₂ showing two possible surface terminations: Pd and CrO₂. Electrons are transferred from Pd layers to CrO₂ layers in the bulk. For the surface CrO₂ layer, only one Pd layer donates electrons to it, resulting in effective hole-doping of the surface layer. Similarly, a surface Pd layer donates electrons to only one CrO₂ layer underneath it, leading to effective electron doping. **b** 3D rendered STM topograph of a freshly cleaved surface of a PdCrO₂ single crystal ($V = 0.8$ V, $I = 50$ pA; image size (30 nm)²). The imaged region comprises a Pd-terminated terrace on the left, a CrO₂-terminated terrace on the right, and a step-edge separating the two. Inset (bottom left), $I(\Delta z)$ curves recorded from the two terraces, showing that the CrO₂

terrace has a larger apparent work function (see also Supplementary Note 1, Supplementary Fig. 1). Inset (top-right), atomically resolved STM image of the CrO₂ terrace showing an unreconstructed (1 × 1) unit cell ($V = 300$ mV, $I = 50$ pA; image size (3 nm)²), scale bar: 1 nm. **c** Spatially resolved soft X-ray photoemission spectroscopy (XPS) map ($h\nu = 110$ eV) taken over the energy range of the Cr 3p and Pd 4p core levels (arrows in **d**) showing shifts in the binding energy of the Cr 3p core level when moving across the sample. **d** Core-level data extracted from the regions in **c** corresponding to the two distinct surface terminations CrO₂ (A: blue region in **c**) and Pd (B: yellow region in **c**).

The alternating +1/−1 nominal valences of the Pd and CrO₂ layers reflect a net charge transfer of one electron from Pd to the neighbouring CrO₂ layers in the bulk (cf. Fig. 1a). The loss of such charge transfer processes at the surface, however, is expected—in a simple ionic picture—to result in an approximately 0.5 holes/Cr (0.5 electrons/Pd) self-doping of the CrO₂ (Pd) terminated surface. Such electronic reconstructions—akin to models for the SrTiO₃/LaAlO₃ interfacial electron gas¹³—have already been observed for the CoO₂-based delafossites, resulting in the stabilization of Rashba-coupled and ferromagnetic metallic surface states on the CoO₂ and Pd terminated surfaces, respectively^{14–18}. For the CrO₂-terminated surface of PdCrO₂, the same mechanism would naively be expected to mediate a substantial doping of 0.5 holes/Cr of the Mott insulating state found in the bulk and drive an insulator-metal transition. In contrast, we show here that the doping triggers a charge-disproportionation in the surface layer, inducing a structural corrugation distinct from the bulk, and driving the surface layer insulating. We further demonstrate that the charge disproportionated state exhibits short-range order and glassy dynamics, evidencing a high degree of degeneracy of the ground state.

Results

Determination of surface termination

Due to the stronger bonding between Cr and O within the CrO₂ octahedra as compared to the bond between oxygen and palladium atoms, PdCrO₂ is expected to cleave between Pd and O. This results in two surface terminations that leave the in-plane order intact—a Pd and a CrO₂ terminated one (Fig. 1a). Consistent with this simple picture, we show in Fig. 1b a topographic scanning tunnelling microscopy (STM, see the “Methods” section) image of the surface of a freshly cleaved sample. The region comprises two flat terraces separated by a step edge. The step height is only ~480 pm, less than the 600 pm expected for adjacent terraces of identical surface termination. This, as well as the different corrugations of the surfaces, suggests that the step edge here is between surfaces of distinct atomic characters. Similarly, the presence of two different surface terminations is also evidenced by our spatially resolved photoemission measurements, performed using a

light spot of ~4 μm in lateral size (see the “Methods” section). The small spot size and typical terrace sizes seen in STM images (see Supplementary Fig. 3), as well as our experience with the surface terminations of other delafossites^{15,16} suggest that in most surface regions, there is no significant inhomogeneity within the probed area. We show in Fig. 1c the spatial variations of the binding energy of the Cr 3p core level, imaged over a region of (400 × 65) μm² of the cleaved surface. Characteristic core-level shifts of ~250 meV are observed, varying between patches of the sample with lateral sizes of ~50–100 μm. The extracted core level spectra integrated over the regions shown in Fig. 1c are shown in Fig. 1d, spanning both the Cr 3p and Pd 4p core levels. The spectrum which exhibits the higher binding energy of the Cr 3p core level (region B, orange line) also exhibits a much more substantial Pd 4p peak, which is almost completely absent in the spectrum from region A (blue line), similar to termination-dependent core-level spectra from the related material AgCrSe₂¹⁹. Both, the core-level shift of the Cr peak as well as the variation of the intensity of the Pd peak allow us to assign region A as CrO₂ terminated and B as Pd terminated. The complete absence of the Pd 4p peak on the CrO₂-terminated areas is likely due to a combination of the lower photoemission cross-section of this peak and the finite probing depth in our measurements. In our atomically-resolved STM data, $I(\Delta z)$ curves (bottom-left inset of Fig. 1b) likewise show different apparent barrier heights for different surface terminations. From the STM data, we assign the surface regions with lower apparent barrier height as Pd-terminated surface regions (region B), and those exhibiting a larger apparent barrier height as CrO₂-terminated areas (region A). These assignments allow us to directly link spectroscopic data between the STM and ARPES data of the two terminations. We will in the following focus on region B, the CrO₂-terminated surface.

Near-Fermi level electronic structure of the CrO₂-terminated surface

The reduced binding energy of the Cr 3p core-level for the CrO₂-terminated surface already provides spectroscopic evidence for the expected hole doping of the surface CrO₂ layer introduced above. To probe the influence of this on the low-energy electronic structure, we

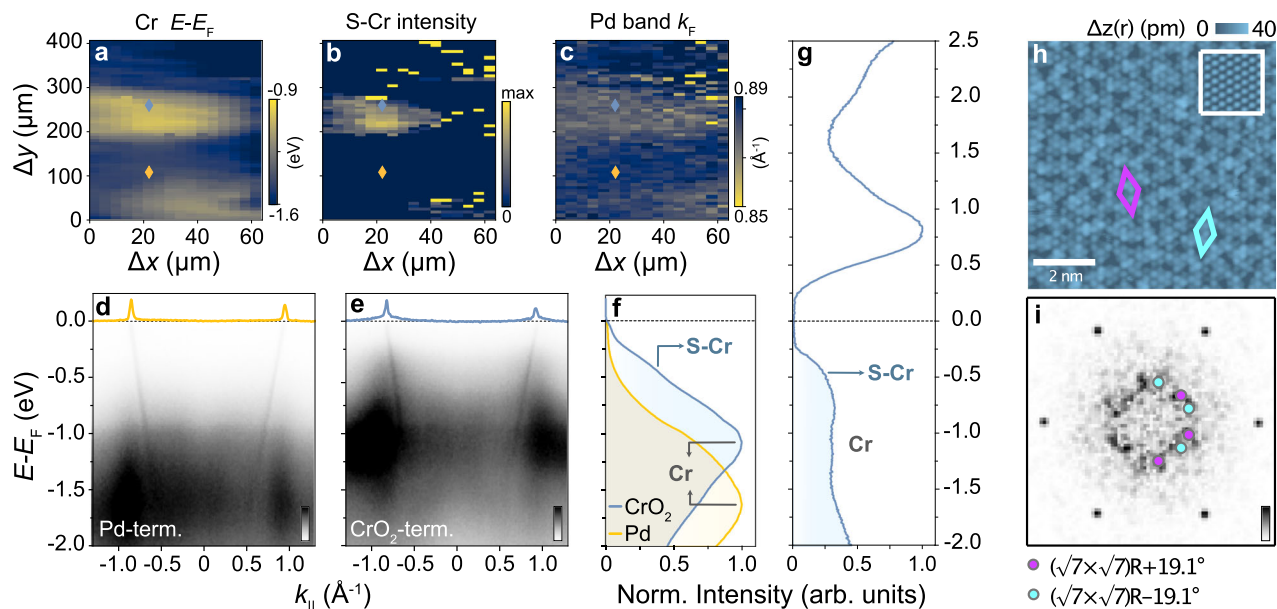


Fig. 2 | Termination-dependent electronic structures. **a–f** Spatially resolved angle-resolved photoemission spectroscopy (ARPES) data of the valence band electronic structure, measured using a photon energy of $h\nu = 110$ eV and linear horizontal (LH) polarized light. Spatially resolved mapping data revealing changes in **a** the binding energy ($E - E_F$) of the Cr-derived peak in the valence band (labelled Cr in **f**), **b** the spectral weight of the Cr-shoulder (S-Cr), and **c** the Fermi wave vector k_F of the steep Pd-derived states, measured across the PdCrO₂ surface over the same region as that in Fig. 1c. **d**, **e** ARPES dispersions of a **d** Pd-terminated (yellow marker in the spatial maps) and **e** CrO₂-terminated (blue marker in the spatial maps) surface region and **f** the k -integrated spectra integrated over the full k -range of the

dispersions shown in **d** and **e**. **g** Differential conductance spectrum $g(V)$ of the CrO₂ terminated surface measured with STM ($V_s = 1.5$ V, $I_s = 50$ pA; $V_m = 10$ mV), showing a shoulder at the same energy as the S-Cr feature in **f**, as well as the upper edge of the surface gap at $+0.25$ eV. **h** Atomically resolved STM topograph of the CrO₂ terminated surface recorded with a bias voltage in the gap near E_F in **g** ($V = 15$ mV, $I = 150$ fA; image size (8 nm)²). Inset, the image at a bias voltage within the peak above E_F in **g** ($V = 350$ mV, $I = 150$ pA; image size (2 nm)²). Coloured rhombi indicate characteristic building blocks of the short-range order with unit cells of $(\sqrt{7} \times \sqrt{7})R \pm 19.1^\circ$ formed locally within the CrO₂ layer. **i** Corresponding Fourier transform of (**h**). Coloured dots mark the FFT peaks of the $(\sqrt{7} \times \sqrt{7})R \pm 19.1^\circ$ order.

show in Fig. 2a–f spatial- and angle-resolved photoemission measurements performed over the same spatial region as the core-level mapping in Fig. 1c. Figure 2d and e show the measured electronic dispersion of a Pd and CrO₂ terminated region, respectively, as identified from our core level mapping in Fig. 1c (see yellow and blue markers in Fig. 2a–c for the measurement positions). In both regions, we find highly dispersive bands derived from the bulk-like Pd states^{6–8}, which cross the Fermi level (E_F) at a Fermi wave vector $k_F \approx \pm 0.87 \text{ \AA}^{-1}$. From the fitting of momentum distribution curves (MDCs) at E_F , we find a small but non-negligible decrease of k_F for the CrO₂ versus the Pd-terminated surface regions (Fig. 2c, Supplementary Fig. 4), indicating a weak hole doping of these Pd-derived states for the CrO₂-terminated surface.

In addition to these metallic states, we observe rather diffuse spectral weight gapped away from E_F , which varies much more significantly between the two surface terminations. We attribute this spectral weight to states of Cr-derived character. For the Pd-terminated regions, this diffuse weight is peaked at a binding energy of ≈ 1.55 eV (evident in the k -integrated spectrum in Fig. 2f), consistent with the location of the lower Hubbard band, which derives from the bulk CrO₂ Mott insulating layer⁸. For the CrO₂-terminated surface, however, we find that this component shifts towards lower binding energies by around 500 meV, while a pronounced shoulder (S-Cr in Fig. 2f) develops closer to the Fermi level at $E - E_F \approx 0.5$ eV. All of these spectral features—the shift to lower binding energy of the dominant Cr-derived density of states (DOS) peak (Fig. 2a), development of spectral weight of the lower-energy shoulder (S-Cr, Fig. 2b), and decrease in k_F of the Pd-derived band (Fig. 2c)—show a spatial dependence that is closely correlated with our identification of CrO₂-derived regions from our core-level spatial mapping (Fig. 1c), indicating that they are characteristic signatures of the electronic structure of the CrO₂-terminated surface.

A direct comparison to our tunnelling spectra measured on the CrO₂-terminated surface, shown in Fig. 2g and Supplementary Fig. 5, reveals similar features. The differential conductance spectrum $g(V)$ shows a clear gap-like structure, with gap edges at ± 0.25 eV, vanishingly small DOS inside the gap, and onset of tunnelling into the occupied states and a broad maximum that is in good agreement with the S-Cr feature observed in ARPES. Taken together, our surface-sensitive spectroscopic measurements thus demonstrate clear modifications in the electronic structure of the CrO₂-terminated surface from that of the Mott-insulating CrO₂ layers of the bulk. Nonetheless, despite the large doping away from half-filling, which is inherent to this polar surface, our measurements show that it remains insulating, defying the simple expectation for such a heavily doped Mott insulator. This suggests that a different form of correlated insulating state is obtained here.

While the differential conductance measured by STM inside the surface gap becomes almost zero, tunnelling through the surface layer to the Pd layer underneath remains possible, although it requires extremely small tunnelling currents (below 500 fA) to achieve stable tunnelling. Excitingly, this enables detailed probing of the correlated states of the surface layer, which would otherwise be extremely challenging for such an insulating layer. Atomically resolved STM measurements performed at a bias voltage of 0.3 V, outside the gap, show an unreconstructed, perfect triangular lattice with a (1 × 1) unit cell (inset in Fig. 1b). We find a notable change in the appearance of this surface topography, however, when imaging the surface at energies inside the gap (Fig. 2h). An additional contrast to that of the regular Cr lattice is evident, which appears rather disordered. The point defects, clearly visible in the topography in Fig. 1b, become virtually invisible when imaged at low energies (see Supplementary Note 5, Supplementary Fig. 6). From the real-space image and its Fourier transform (Fig. 2i), we can identify a characteristic length scale, indicating the

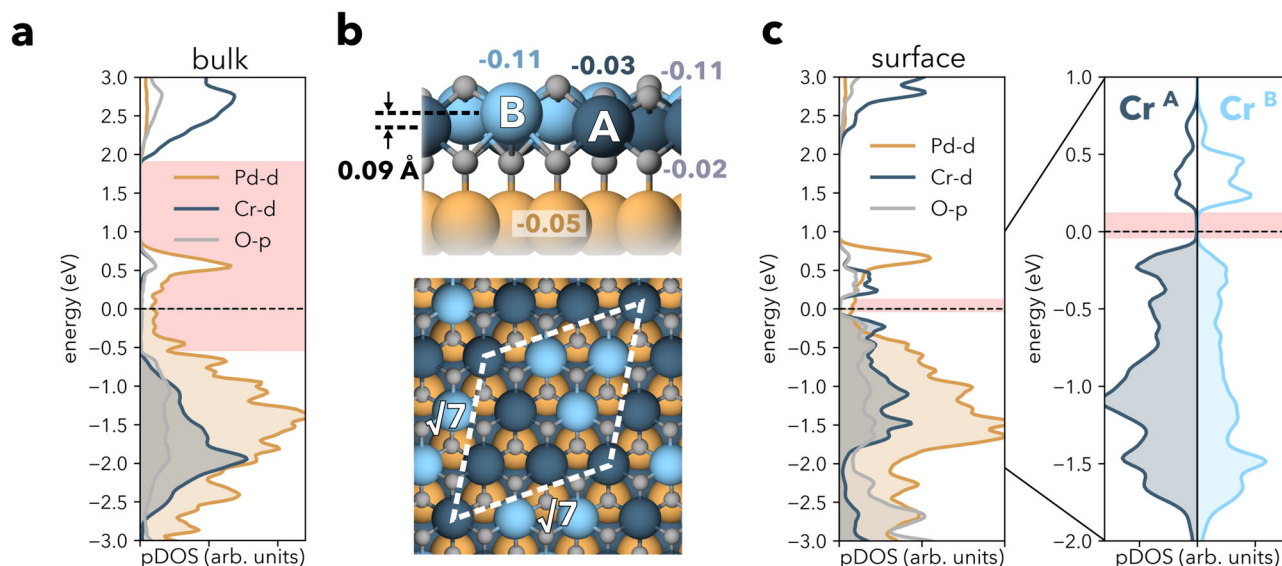


Fig. 3 | Modelling of the CrO₂ surface. **a** Projected density of states (PDOS) of bulk PdCrO₂ modelled with $\sqrt{7} \times \sqrt{7}$ unit cell and a collinear configuration of 4 spin-up and 3 spin-down Cr atoms (see the “Methods” section), exhibiting the metallic nature of Pd states and the hidden Mott insulating nature of CrO₂ layers (the gap is emphasized with red stripe). **b** CrO₂ surface modelled with the same unit cell and relaxed, showing a vertical displacement of Cr atoms of up to 0.1 Å and resulting in two distinct types of Cr atoms, Cr^A and Cr^B. The numbers near spheres represent the

difference in electronic charge of the atoms at the surface from those in the bulk obtained from a Bader analysis (negative values reflect hole doping). **c** PDOS of the CrO₂ surface. The states at E_F are derived from the subsurface Pd layer, whereas the Cr *t*_{2g} states are gapped by -0.2 eV, with Cr^B more strongly hole-doped than Cr^A. The inset to the right shows the PDOS for Cr^A and Cr^B for a narrower energy range around the Fermi energy.

formation of a short-range ordered state. From the dominant features in the Fourier transform, we identify the basic building block of this short-range order as a $(\sqrt{7} \times \sqrt{7})R \pm 19.1^\circ$ unit.

Formation of a charge disproportionated insulator

To understand why the surface layer remains insulating, despite the significant charge transfer and the origins of its peculiar local order, we have modelled a PdCrO₂ slab and performed spin-polarized density functional theory (DFT) calculations. We use a DFT + *U* scheme to include the effect of correlations—a calculation scheme that we find well reproduces the hidden Mott gap of the bulk electronic structure, Fig. 3a (see Supplementary Note 6 for details).

We have modelled the CrO₂ surface by a slab containing three Pd and four CrO₂ layers in a $\sqrt{3} \times \sqrt{3}$ unit cell enclosed by a vacuum. Calculations using such a slab, including relaxation, stabilize a ferromagnetic ground state in the surface CrO₂ layer that is metallic—as expected for a heavily-doped Mott insulator, but clearly inconsistent with our spectroscopic data. To address this discrepancy, we introduce the peculiar $\sqrt{7} \times \sqrt{7}$ order observed in our STM measurements into the calculations by creating a unit cell containing seven Cr atoms per layer. Relaxing the atomic positions in this unit cell results in a structural modification of the surface layer, which leads to two distinct types of Cr atoms, Cr^A and Cr^B, which are distributed with a 4:3 ratio and arranged in a pattern as depicted in Fig. 3b.

Cr atoms of both types relax outwards at the surface but by different amounts. The relaxation results in an off-centring of the Cr atoms within the surface CrO₆ octahedra, by 0.06 and 0.14 Å for Cr^A and Cr^B atoms, respectively, with the larger out-of-plane relaxation of Cr^B accompanied by a larger distortion of the octahedra. The difference of -0.1 Å in the height of the two Cr species provides a natural explanation for the contrast in the STM images evident in Fig. 2h (compare also Supplementary Fig. 10 for simulated STM images).

Most strikingly, this structural distortion renders the surface insulating, stabilizing a full gap of -0.2 eV within the Cr *t*_{2g} manifold, as depicted in Fig. 3c. In agreement with our STM and ARPES measurements, this gap is substantially smaller when compared to the bulk gap

which separates the *t*_{2g} and *e*_g manifolds. This is in stark contrast with calculations for an unreconstructed surface, where DFT calculations yield a metallic state (see Supplementary Note 8).

The key question is, therefore, why the CrO₂ surface avoids such a metallic state and how the insulating state results in the reconstructed surface layer. In a purely ionic picture (Fig. 1a), simple electron counting would suggest that the 0.5 hole/Cr doping of the surface layer could be accommodated via a charge ordering of the Cr sites, with equal numbers of *d*² and *d*³ occupancies to give an average *d*^{2.5} configuration. In line with this picture, we find that the charges in the surface CrO₂ layer redistribute laterally, resulting in Cr^A atoms containing more electrons in their *t*_{2g} manifold than Cr^B atoms (upper panel in Fig. 3b). This is reflected by a higher magnetic moment of the Cr^A sites of 2.83 μ_B (close to the 2.89 μ_B of the bulk) as compared to 2.49 μ_B of the Cr^B atoms. A Bader charge analysis provides additional support for such a picture, with Cr^A (Cr^B) atoms having 0.03 (0.11) fewer electrons than the Cr atoms in the bulk (Fig. 3b). The Pd atoms in the layer underneath remain non-magnetic and with the same charge throughout. The charge disproportionation that occurs in the surface CrO₂ layer only happens once the on-site Coulomb interaction is added to the Cr 3*d* electrons through the Hubbard-like *U* term, suggesting a critical role of electron correlations. We also note that, because the wave functions are delocalized also over the oxygen atoms, an additional contribution to the charge order might also come from the oxygen ligands.

Indeed, our analysis indicates that the additional surface charge is not purely accommodated by the surface Cr atoms. The topmost oxygen atoms, sitting above the Cr layer, have fewer electrons than those in the bulk (Fig. 3b). Furthermore, the doping is not confined exclusively to the surface CrO₂ layer, and we find a slight hole doping (0.05 holes/Pd) for the subsurface Pd layer, as evidenced by a shift of its Pd band crossing E_F by -0.1 eV towards lower binding energies compared to the Pd bands in deeper layers (see Supplementary Note 10, Supplementary Fig. 13a, b). In consequence, there are less than 0.5 holes/Cr left to be distributed among the Cr atoms and slightly more than half of the Cr atoms (Cr^A) stay in a bulk-like *d*³ configuration

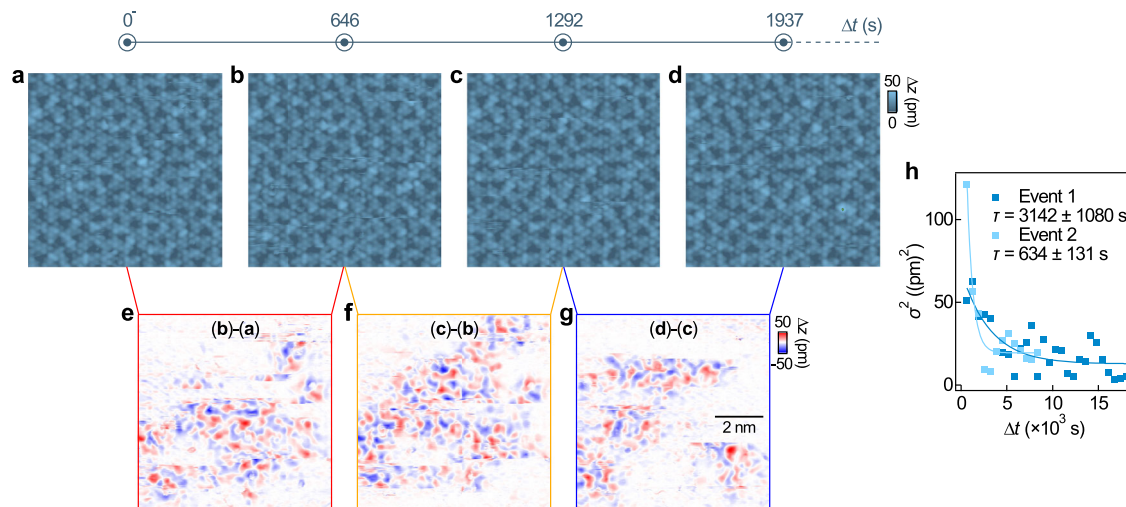


Fig. 4 | Dynamics of the glassy state in the surface CrO₂ layer. **a–d** Atomically resolved images of the CrO₂-terminated surface taken **(a)** before and **(b)–(d)** after a 70 mV voltage pulse with a duration of 2 s were applied in the centre of the image. ($V = 5$ mV, $I = 150$ fA, image size: $(8 \text{ nm})^2$). The time Δt after the voltage pulse at which the images were obtained is indicated. **e–g** Difference of consecutive images

shown in **(a)–(d)** reveal the dynamics of the charge ordered state following the voltage pulse. **h** Scatter plot of the variance of the height distribution in the difference images as a function of Δt . An exponential fit to the data recorded from two individual experiments reveals relaxation time constants (τ) of -3140 ± 1080 s (dark blue) and -634 ± 131 s (light blue), respectively.

(as inferred from their magnetic moment), while the remainder of the Cr atoms (Cr^B) end up in a configuration as close as possible to d^2 . This charge disproportionation lowers the energy when compared to a metallic state, where charges are delocalized and homogeneously distributed among the atoms of the same species. The charge disproportionation further results in the gapping of the electronic states. The Mott gap becomes replaced by a charge gap driven by the localization of charge carriers and Coulomb repulsion. Other mechanisms, such as the formation of a charge density wave, would not result in complete gapping of the Fermi surface.

The charge disproportionation and the accompanying structural modification are thus instrumental in avoiding metallicity and maintaining the insulating nature of the surface CrO₂ layer. Also, we find that details of the magnetic order on the Cr atoms only affect the size of the gap, but not its presence, hence suggesting that charge disproportionation is the primary driver for the insulating ground state (see Supplementary Note 8, Supplementary Fig. 12). In this respect, we note that, for the bulk, the opening of the Mott gap does not require magnetism to be included in calculations once correlation effects are properly accounted for^{12,20}. The robustness of the gap in the surface layer to details of the magnetic order suggests that the situation there mirrors that in the bulk, and treatments with methods that account more realistically for correlation effects may yield an insulating state without magnetic order.

Glassy dynamics

While our calculations and experiments demonstrate that the doped Mott layer at the surface of PdCrO₂ forms a charge-disproportionated insulator, both data and experiments also point towards a competition of ground states with similar periodicity. In the experiments, this is evidenced by the short-ranged nature of the order, suggesting that it is frustrated and only presents a shallow energy minimum, while in calculations, a number of different magnetic ground states are close by in energy. In STM images, the structural modification can only be imaged at extremely small tunnelling currents $I \sim 150$ fA (Fig. 2h), whereas using higher currents triggers changes in the order and STM images appear fuzzy (see Supplementary Note 10, Supplementary Fig. 14, also Supplementary Fig. 6), suggesting that the ground state is susceptible to small perturbations.

Moreover, we find that changes in the surface order can be triggered through deliberate voltage pulses, disrupting the short-range order as seen through changes in the topographic appearance imaged at very low tunnelling currents. The system slowly relaxes towards a new equilibrium, enabling us to study the resulting temporal dynamics of the system. Figure 4 shows such a measurement series. In Fig. 4a, we show the appearance of the short-range order of the surface layer before applying a voltage pulse in the centre of the image. Figure 4b–d shows the time evolution after the voltage pulse has been applied. The images have all been recorded in the same spatial location, with changes in the image contrast reflecting a reconfiguration of the short-range order. Figure 4e–g shows the difference images of the topographic measurements recorded at consecutive time points to highlight the changes.

An analysis of the temporal behaviour from difference images, such as the ones shown in Fig. 4e–g, is shown in Fig. 4h. We find that the relaxation dynamics follow an exponential behaviour with a time constant on the order of tens of minutes. This indicates a slow characteristic timescale over which the system settles following excitation. Moreover, our data indicates that the system relaxes to a different state than the one before the trigger (see Supplementary Note 11, Supplementary Fig. 15). This suggests that the ground state here is only metastable and is characterized by glassy behaviour.

Discussion

Our study reveals a surprising resilience of the insulating state of the CrO₂ surface layer in the hidden Mott insulator PdCrO₂ to pronounced charge carrier doping away from half-filling. We show how, in the CrO₂ surface layer, a glassy state is formed, developing from a charge-disproportionated insulating ground state. The gap of this state could easily be taken for that of a Mott insulator at half-filling²¹, which, however, is not expected here due to the significant charge transfer occurring near the surface. The formation of a charge disproportionation is unexpected here because it occurs in a metal, supporting a description of the system as a heterostructure combining layers with disparate ground states that are largely—although not completely⁸—decoupled, with the screening that would counteract charge disproportionation sufficiently localized in the Pd layer here.

The short-range nature of the charge order and its glassy dynamics suggest a high level of frustration with the relevant interactions and a ground state that is close in energy to multiple nearly degenerate metastable states. The occurrence of charge-ordered states has been widely discussed for the Hubbard model on a square lattice for the cuprates, where a spin-charge separation has been predicted²² and observed²³ for characteristic dopings, and which exhibit charge-density-wave order in the underdoped material^{24,25}. Here, the charge order occurs at significantly higher doping and results in a fully insulating state. This motivates further studies of the CrO₂ surface layer, in particular if the charge doping in the surface layer can be further modified by surface doping methods. An interesting question is whether a metallic state can then be recovered. This would provide an exciting platform to study the phase diagram of the resulting correlated states when doping a Mott insulator on a triangular lattice. The metallicity of the sub-surface Pd layer here further ensures that the multi-orbital Mott–Hubbard physics remains accessible for state-of-the-art surface spectroscopies. Such a platform would enable searching for the formation of long-range ordered states, exploring the metal-insulator transition, the interplay with the putative ferromagnetic metal state, as well as searching for the possible emergence of unconventional superconductivity.

Methods

Crystal growth

Single-crystal samples of PdCrO₂ were grown by the NaCl-flux method as reported in ref. 10. First, polycrystalline PdCrO₂ powder was prepared from the following reaction at 960 °C for four days in an evacuated quartz ampoule:



The obtained powder was washed with water and aqua regia to remove LiCl. The polycrystalline PdCrO₂ and NaCl were mixed in the molar ratio of 1:10. Then, the mixture in a sealed quartz tube was heated at 900 °C and slowly cooled down to 750 °C. PdCrO₂ single crystals were harvested after dissolving the NaCl flux with water.

Scanning tunnelling microscopy/spectroscopy

The STM experiments were performed using a home-built low-temperature STM that operates at a base temperature of 1.8 K²⁶. Pt/Ir tips were used and conditioned by field emission with a gold target. The bias voltage V is applied to the sample with the tip at virtual ground. Differential conductance ($g(\mathbf{r}, V)$) maps and single point $g(V)$ spectra were recorded using a standard lock-in technique, with the frequency of the bias modulation set at 413 Hz. To obtain a clean surface for STM measurements, PdCrO₂ samples were cleaved in situ at temperatures below -20 K in cryogenic vacuum. Measurements were performed at a sample temperature of 4.2 K unless stated otherwise. To be able to image within the surface gap (Fig. 2h), extremely small currents down to about 100 fA have to be used.

μ -ARPES

The single crystal samples were cleaved in situ at a base pressure lower than 10⁻¹⁰ mbar. The photoemission measurements were performed using the nano-ARPES branch of the I05 endstation at Diamond Light Source, UK. The light was focussed onto the sample using a reflective capillary optic, which provides a spot size of ~4 μm . The sample was mounted on a five-axis manipulator with piezoelectrically-driven axes used for spatial mapping of the sample. The emitted photoelectrons were detected using a Scienta Omicron DA30 analyser. All measurements were taken at a base temperature of ~40 K, using p -polarized light with photon energies of $h\nu = 110$ eV for the valence band spectra and $h\nu = 150$ eV for the core level mapping.

Computational details

Density functional theory (DFT) calculations were performed using the VASP package²⁷. Bulk PdCrO₂ was modelled assuming the $R\bar{3}m$ space group and using the experimental lattice structure obtained from neutron diffraction at room temperature ($a = 2.9280$ Å, $c = 18.1217$ Å, $z = 0.11057$) with atoms placed at Pd 3a (0, 0, 0), Cr 3b (0, 0, 0.5), and O 6c (0, 0, z) positions¹¹. We used the unit cell containing six PdCrO₂ layers and having the $\sqrt{3} \times \sqrt{3}$ in-layer periodicity (3 Cr atoms per layer) to allow for the modelling of different antiferromagnetic spin arrangements on a triangular Cr lattice.

As discussed in the literature, the correct description of the Mott-insulating electronic structure of CrO₂ layers in bulk PdCrO₂ requires either the use of a combination of DFT with Dynamic Mean Field Theory (DFT + DMFT) or the extension of the DFT treatment with Hubbard U (and Hund J) terms added to the Cr 3d orbitals (DFT + U method)^{12,28,29}. We turned to the second option, which is computationally more affordable and allows treating the surfaces. We used the Perdew–Burke–Ernzerhof (PBE) exchange-correlation functional³⁰ and the rotationally invariant DFT + U approach of Dudarev³¹ with parameters $U = 4$ eV and $J = 0.9$ eV which showed the best agreement with experiments and DMFT calculations^{8,12}. The details justifying this particular choice of U and J values are discussed in Supplementary Note 6. The plane wave cutoff was set to 350 eV, and the self-consistent field calculations were performed on a (8, 8, 1) mesh of k -points.

The CrO₂ surface was modelled using a symmetric slab containing three Pd and four CrO₂ layers, terminated by CrO₂ layers on both ends, in a $\sqrt{7} \times \sqrt{7}$ unit cell. This choice of the unit cell is motivated by our STM measurements, which showed a peculiar $\sqrt{7} \times \sqrt{7}$ periodicity of the surface. Because the structural optimization of large systems in noncollinear approach is burdensome and often leads to numerical instabilities, we turned to computationally more affordable spin-polarized DFT calculations, neglecting spin-orbit coupling. We checked that the bulk hidden Mott gap is reproduced in these calculations (Supplementary Fig. 9). The magnetic moments on Cr atoms in a spin-polarized approach are distributed as follows: the first layer (at the bottom) contains four $+3\mu_B$ and three $-3\mu_B$ magnetic moments, the second layer three $+3\mu_B$ and four $-3\mu_B$, and the third layer has again four $+3\mu_B$ and three $-3\mu_B$. Within a $\sqrt{7} \times \sqrt{7}$ unit cell, such a spin configuration is the closest possible approximation to the AF ordering. Concerning the surface CrO₂ layer (the top layer), we tried a few different initial spin configurations and fully relaxed the atomic positions until the forces on all the atoms from the surface CrO₂ and subsurface Pd layer dropped below 0.005 eV/Å. The atoms from the other layers are kept fixed in their positions. While the gap in the surface layer is observed for different spin configurations (Supplementary Fig. 12), Supplementary Fig. 11 shows that it only opens once the structural modification of the surface layer is accounted for, but not in the unrelaxed surface. We used a (3, 3, 1) k -mesh to perform the structural relaxation and a (6, 6, 1) k -mesh for subsequent self-consistent field calculations. The (P)DOS plots are produced with the VASPKIT code³². Band structure unfolding onto the primitive cell was performed using the b4vasp package³³. STM images were simulated using the Critic2 package³⁴. Structural setup and visualization were performed using the Atomic Simulation Environment package³⁵.

Data availability

Underpinning data will be made available online at ref. 36.

References

- Anderson, P. W. Resonating valence bonds: a new kind of insulator? *Mater. Res. Bull.* **8**, 153–160 (1973).
- Balents, L. Spin liquids in frustrated magnets. *Nature* **464**, 199–208 (2010).

3. Kourtis, S., Venderbos, J. W. F. & Daghofer, M. Fractional Chern insulator on a triangular lattice of strongly correlated t_{2g} electrons. *Phys. Rev. B* **86**, 235118 (2012).
4. Venderbos, J. W. F., Kourtis, S., Brink, J. van den. & Daghofer, M. Fractional quantum-Hall liquid spontaneously generated by strongly correlated t_{2g} electrons. *Phys. Rev. Lett.* **108**, 126405 (2012).
5. Ong, N. P. Physics: electronic frustration on a triangular lattice. *Science* **305**, 52–53 (2004).
6. Sobota, J. A. et al. Electronic structure of the metallic antiferromagnet PdCrO₂ measured by angle-resolved photoemission spectroscopy. *Phys. Rev. B* **88**, 125109 (2013).
7. Noh, H.-J. et al. Direct observation of localized spin antiferromagnetic transition in PdCrO₂ by angle-resolved photoemission spectroscopy. *Sci. Rep.* **4**, 3680 (2014).
8. Sunko, V. et al. Probing spin correlations using angle-resolved photoemission in a coupled metallic/Mott insulator system. *Sci. Adv.* **6**, eaaz0611 (2020).
9. Mackenzie, A. P. The properties of ultrapure delafossite metals. *Rep. Prog. Phys.* **80**, 032501 (2017).
10. Takatsu, H. & Maeno, Y. Single crystal growth of the metallic triangular-lattice antiferromagnet PdCrO₂. *J. Cryst. Growth* **312**, 3461–3465 (2010).
11. Takatsu, H. et al. Magnetic structure of the conductive triangular-lattice antiferromagnet PdCrO₂. *Phys. Rev. B* **89**, 104408 (2014).
12. Lechermann, F. Hidden Mott insulator in metallic PdCrO₂. *Phys. Rev. Mater.* **2**, 085004 (2018).
13. Nakagawa, N., Hwang, H. Y. & Muller, D. A. Why some interfaces cannot be sharp. *Nat. Mater.* **5**, 204–209 (2006).
14. Kim, K., Choi, H. C. & Min, B. I. Fermi surface and surface electronic structure of delafossite PdCoO₂. *Phys. Rev. B* **80**, 035116 (2009).
15. Sunko, V. et al. Maximal Rashba-like spin splitting via kinetic-energy-coupled inversion-symmetry breaking. *Nature* **549**, 492–496 (2017).
16. Mazzola, F. et al. Itinerant ferromagnetism of the Pd-terminated polar surface of PdCoO₂. *PNAS* **115**, 12956–12960 (2018).
17. Yim, C. M. et al. Quasiparticle interference and quantum confinement in a correlated Rashba spin-split 2D electron liquid. *Sci. Adv.* **7**, eabd7361 (2021).
18. Mazzola, F. et al. Tuneable electron-magnon coupling of ferromagnetic surface states in PdCoO₂. *npj Quantum Mater.* **7**, 20 (2022).
19. Siemann, G.-R. et al. Spin-orbit coupled spin-polarised hole gas at the CrSe₂-terminated surface of AgCrSe₂. *npj Quantum Mater.* **8**, 61 (2023).
20. Lechermann, F. From basic properties to the Mott design of correlated delafossites. *npj Comput. Mater.* **7**, 1–17 (2021).
21. Wen, C. et al. Probing Hidden Mott gap and incommensurate charge modulation on the polar surfaces of PdCrO₂. *Phys. Rev. Lett.* **131**, 116501 (2023).
22. Zaanen, J. & Gunnarsson, O. Charged magnetic domain lines and the magnetism of high- T_c oxides. *Phys. Rev. B* **40**, 7391–7394 (1989).
23. Emery, V. J., Kivelson, S. A. & Tranquada, J. M. Stripe phases in high-temperature superconductors. *Proc. Natl Acad. Sci. USA* **96**, 8814–8817 (1999).
24. Kohsaka, Y. et al. An intrinsic bond-centered electronic glass with unidirectional domains in underdoped cuprates. *Science* **315**, 1380–1385 (2007).
25. Cai, P. et al. Visualizing the evolution from the Mott insulator to a charge-ordered insulator in lightly doped cuprates. *Nat. Phys.* **12**, 1047–1051 (2016).
26. White, S. C., Singh, U. R. & Wahl, P. A stiff scanning tunneling microscopy head for measurement at low temperatures and in high magnetic fields. *Rev. Sci. Instrum.* **82**, 113708 (2011).
27. Kresse, G. & Joubert, D. From ultrasoft pseudopotentials to the projector augmented-wave method. *Phys. Rev. B* **59**, 1758–1775 (1999).
28. Le, ManhDuc et al. Magnetic interactions in PdCrO₂ and their effects on its magnetic structure. *Phys. Rev. B* **98**, 024429 (2018).
29. Billington, D. et al. Magnetic frustration, short-range correlations and the role of the paramagnetic Fermi surface of PdCrO₂. *Sci. Rep.* **5**, <https://doi.org/10.1038/srep12428> (2015).
30. Perdew, J. P., Burke, K. & Ernzerhof, M. Generalized gradient approximation made simple. *Phys. Rev. Lett.* **77**, 3865–3868 (1996).
31. Dudarev, S. L., Botton, G. A., Savrasov, S. Y., Humphreys, C. J. & Sutton, A. P. Electron-energy-loss spectra and the structural stability of nickel oxide: an LSDA + U study. *Phys. Rev. B* **57**, 1505–1509 (1998).
32. Wang, V., Xu, N., Liu, J.-C., Tang, G. & Geng, W.-T. Vaspkit: a user-friendly interface facilitating high-throughput computing and analysis using VASP code. *Comput. Phys. Commun.* **267**, 108033 (2021).
33. Dirnberger, D., Kresse, G., Franchini, C. & Reticcioli, M. Electronic state unfolding for plane waves: energy bands, Fermi surfaces, and spectral functions. *J. Phys. Chem. C* **125**, 12921–12928 (2021).
34. Roza, A. O.-de-la., Johnson, E. R. & Luaña, V. Critic2: a program for real-space analysis of quantum chemical interactions in solids. *Comput. Phys. Commun.* **185**, 1007–1018 (2014).
35. Larsen, A. H. et al. The atomic simulation environment—a Python library for working with atoms. *J. Phys.: Condens. Matter* **29**, 273002 (2017).
36. Yim, C. M. et al. Avoided metallicity in a hole-doped Mott insulator on a triangular lattice (dataset). University of St Andrews Research Portal <https://doi.org/10.17630/39eac936-f4f0-4245-a247-7a9ff44c8e21> (2024).

Acknowledgements

We thank Sota Kitamura, Takashi Oka, Masafumi Udagawa and Hidetomo Usui for useful discussions and preliminary calculations. We gratefully acknowledge support from the UK Engineering and Physical Sciences Research Council (Grant Nos. EP/S005005/1 and EP/T02108X/1), the European Research Council (through the QUESTDO project, 714193), the Leverhulme Trust (Grant No. RL-2016-006), the Royal Society through the International Exchange grant IEC\R2\222041 and the Italian Ministry of Research through the PRIN-2022 “SORBET” project No.2022ZY8HJY. C.M.Y. acknowledges support from Shanghai Pujiang Talent Programme 21PJ1405400 and TDLI Start-up Fund. S.S. acknowledges the financial support provided by the Ministry of Education, Science, and Technological Development of the Republic of Serbia. S.S. and S.P. acknowledge the CINECA award under the ISCRA initiative, for the availability of high-performance computing resources and support. We thank Diamond Light Source for access to the I05 beamline (Proposal No. SI28445), which contributed to the results presented here.

Author contributions

C.M.Y. performed the STM experiments. G.R.S., P.A.E.M., T.A., and P.D.C.K. performed the ARPES experiments. S.S. and S.P. performed theoretical modelling. S.K. and A.P.M. provided samples. C.M.Y. analysed the STM data, and G.R.S. the ARPES data. I.B. performed preliminary calculations. M.D.W. maintained the Diamond I05 nano-ARPES beamline and provided experimental support. C.M.Y., G.R.S., S.S., S.P., P.D.C.K., and P.W. wrote the manuscript. All authors discussed the manuscript. The project was initiated by P.W., P.D.C.K., and A.P.M.

Competing interests

The authors declare no competing interests.

Additional information

Supplementary information The online version contains supplementary material available at <https://doi.org/10.1038/s41467-024-52007-z>.

Correspondence and requests for materials should be addressed to Chi Ming Yim, Silvia Picozzi, Phil D. C. King or Peter Wahl.

Peer review information *Nature Communications* thanks Yingshuang Fu, and the other, anonymous, reviewers for their contribution to the peer review of this work. A peer review file is available.

Reprints and permissions information is available at <http://www.nature.com/reprints>

Publisher's note Springer Nature remains neutral with regard to jurisdictional claims in published maps and institutional affiliations.

Open Access This article is licensed under a Creative Commons Attribution 4.0 International License, which permits use, sharing, adaptation, distribution and reproduction in any medium or format, as long as you give appropriate credit to the original author(s) and the source, provide a link to the Creative Commons licence, and indicate if changes were made. The images or other third party material in this article are included in the article's Creative Commons licence, unless indicated otherwise in a credit line to the material. If material is not included in the article's Creative Commons licence and your intended use is not permitted by statutory regulation or exceeds the permitted use, you will need to obtain permission directly from the copyright holder. To view a copy of this licence, visit <http://creativecommons.org/licenses/by/4.0/>.

© The Author(s) 2024

Supporting Information for "Avoided metallicity in a hole-doped Mott insulator on a triangular lattice"

Chi Ming Yim^{*,1,2,†} Gesa-R. Siemann^{*,1} Srdjan Stavrić^{*,3,4} Seunghyun Khim,⁵ Izidor Benedičič,¹ Philip A. E. Murgatroyd,¹ Tommaso Antonelli,¹ Matthew D. Watson,⁶ Andrew P. Mackenzie,^{1,5} Silvia Picozzi,^{3,‡} Phil D.C. King,^{1,§} and Peter Wahl^{1,7,¶}

¹*SUPA, School of Physics and Astronomy,
University of St Andrews, North Haugh,
St Andrews, Fife, KY16 9SS, United Kingdom*

²*Tsung Dao Lee Institute and School of Physics and Astronomy,
Shanghai Jiao Tong University, Shanghai, 201210, China*

³*Consiglio Nazionale delle Ricerche (CNR-SPIN),
Unità di Ricerca presso Terzi c/o Università "G. D'Annunzio", 66100 Chieti, Italy*

⁴*Vinča Institute of Nuclear Sciences - National Institute of the Republic of Serbia,
University of Belgrade, P. O. Box 522, RS-11001 Belgrade, Serbia*

⁵*Max Planck Institute for Chemical Physics of Solids,
Nöthnitzer Straße 40, 01187 Dresden, Germany*

⁶*Diamond Light Source, Harwell Science and Innovation Campus,
Didcot, OX11 0DE, United Kingdom*

⁷*Physikalisches Institut, Universität Bonn,
Nussallee 12, 53115 Bonn, Germany*

(Dated: August 12, 2024)

* These authors contributed equally.

[†]Electronic address: c.m.yim@sjtu.edu.cn.

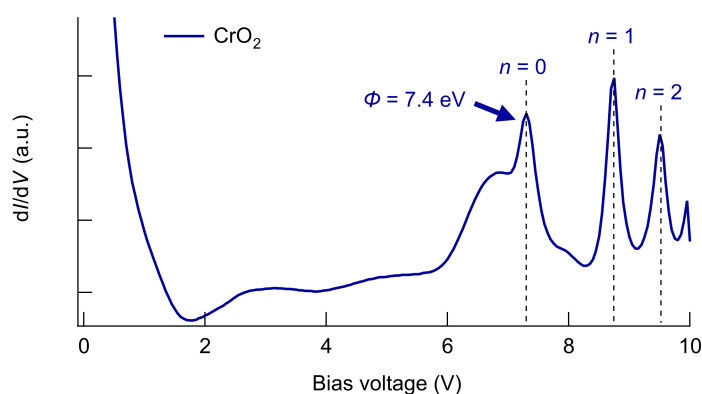
[‡]Electronic address: silvia.picozzi@spin.cnr.it

[§]Electronic address: pdk6@st-andrews.ac.uk

[¶]Electronic address: wahl@st-andrews.ac.uk

Supplementary note 1. Determination of the surface work function of the CrO₂-terminated surface

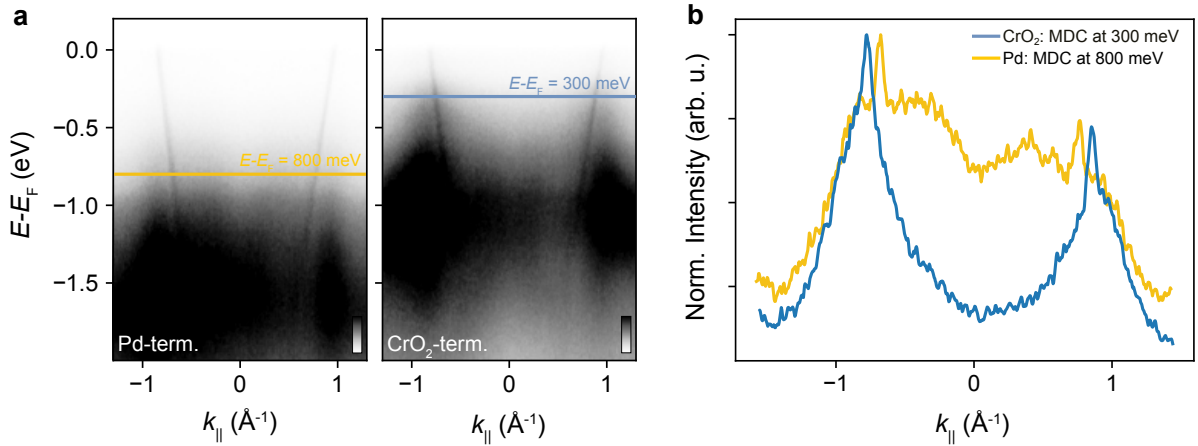
We have measured the image potential states of the CrO₂-terminated surface, achieved by measuring the differential conductance $g(V)$ as a function of bias voltage V in a closed loop condition. Fig. S1 shows such a $g(V)$ spectrum recorded from a defect-free position of the CrO₂-terminated surface, in which the position of the lowest order peak ($n = 0$) can be taken as an approximation of the surface work function. We have therefore determined that the CrO₂-terminated surface has a surface work function of 7.4eV, very close to that of the CoO₂ termination of PdCoO₂.¹



Supplementary Figure S1: **Measurement of work function of the CrO₂- terminated surface of PdCrO₂.** Point $g(V)$ spectrum recorded with closed feedback-loop from the CrO₂ surface termination ($I_s = 10\text{pA}$; $V_m = 50\text{mV}$). The arrow marks the lowest order peak of the standing-wave states, the energy position of which approximates the surface work function ϕ .

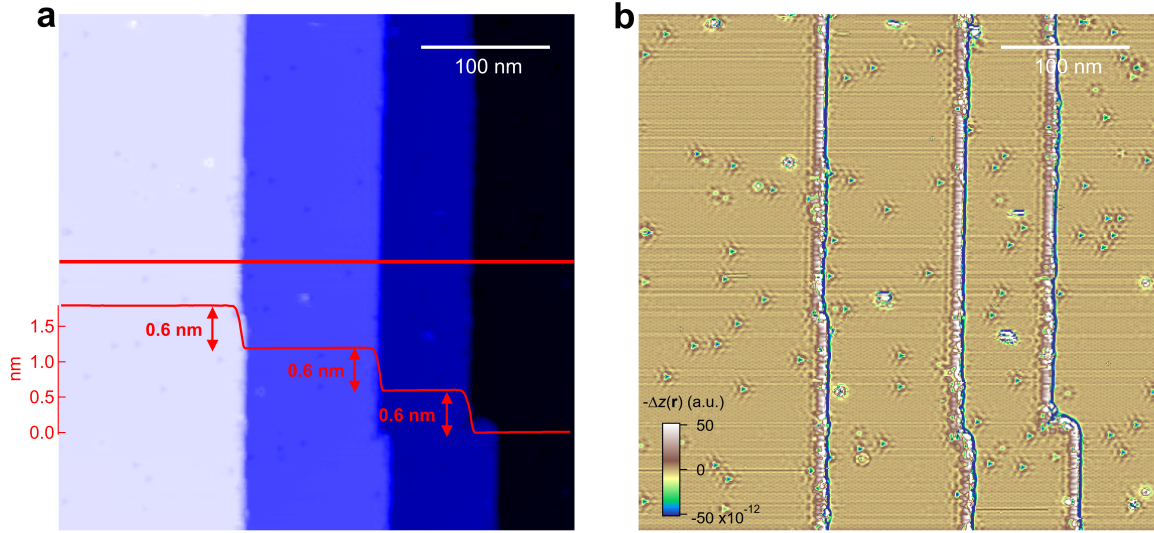
Supplementary note 2. Surface homogeneity

While cleaving the samples results in areas with different surface terminations and could, in principle, also result in inhomogeneity with each surface termination, from our data as well as experience with measurements on the surfaces of other delafossite oxides we have ample evidence that the areas we have investigated are dominated by a single homogeneous termination. We have extensively characterised the distinct terminations of the cleaved surfaces of the family of (Pd, Pt)(Co, Cr)O₂ compounds. In the Co-based systems, extremely clear signatures of



Supplementary Figure S2: **Termination-dependent ARPES measurements.** Comparison of the extracted momentum distribution curves (MDCs) from the two surface regions (labelled Pd- and CrO₂ in (a)) at different binding energies ($E - E_F$) as indicated by the solid lines in the spectra shown in (a). Clear differences can be seen in the extracted MDCs separated by an energy difference of 500 meV, ruling out that these spectra from the different surface terminations can be understood simply via a rigid band shift.

electron- and hole- doping of the CoO₂ and (Pd, Pt) surface terminations can be observed, with clear-cut spectral signatures that easily allow identifying any minority/mixed terminations^{2,3}, and again consistent between ARPES and STM^{1,4}. In such measurements, we have observed well-defined surface terminations with length scales $\gg 50\mu\text{m}$, entirely consistent with the length scale of the variations that we assign here for the CrO₂- and Pd-terminated surfaces. With similar variations also in core-level spectra, and spectra that cannot be simply reproduced via a rigid band shift (Supplementary Figure S2), we are confident in similarly assigning the observed patches here as Pd- and CrO₂- terminated regions, with minimal contribution from charge puddles due to excess Pd impurities. This does not mean that the surface terminations are atomically flat over this probing region. Indeed, large scale topographic images as shown in Figure S3(a) are characterised by flat terraces separated by step edges running along the same direction. The line profile taken across the terraces shows clearly that the terraces are separated from each other by the same step height of $\sim 600\text{pm}$, indicating that all the terraces are of the same (here CrO₂) termination. Importantly, there is negligible sign within the probing region of spatially varying inhomogeneity as can be seen in the negative Laplacian of the topography

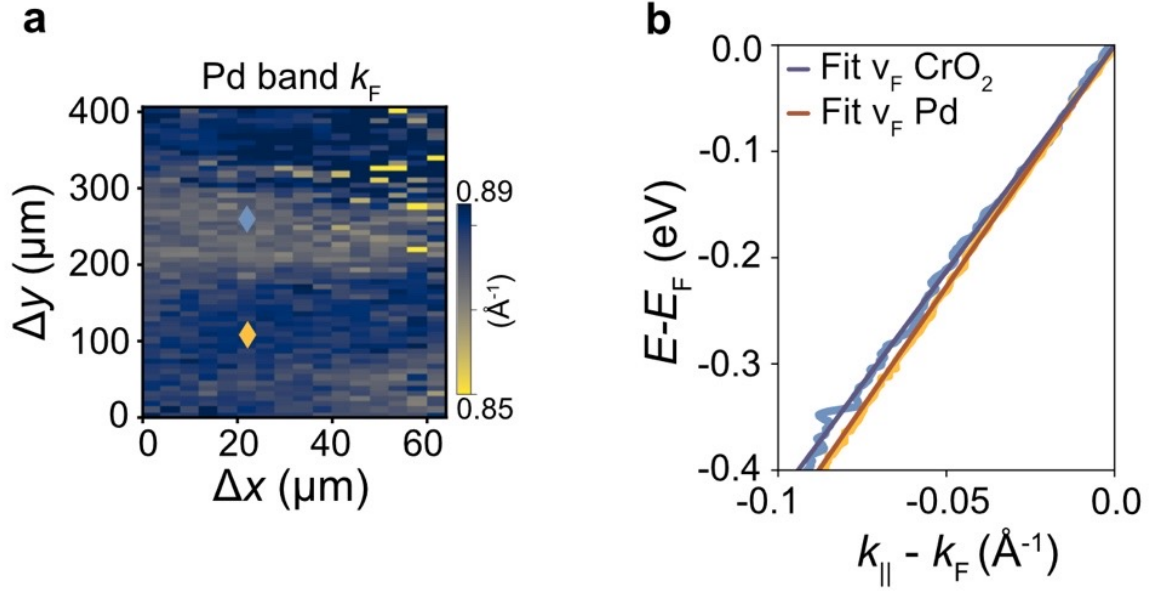


Supplementary Figure S3: **Large-scale STM image.** (a) STM image with a lateral size of $400 \times 400 \text{ nm}^2$, showing multiple terraces with the same CrO_2 termination and a very high surface homogeneity ($V = 1.5 \text{ V}$, $I = 0.1 \text{ nA}$). (b) Negative Laplacian of the topographic image in (a).

in Figure S3(b).

Supplementary note 3. Sub-surface charge transfer

The small changes in k_F evident in fig. 2c of the main text for the bulk-like Pd states measured at the Pd vs. the CrO_2 -terminated surface point to a small charge transfer from the CrO_2 -terminating surface to the subsurface Pd layer. In Figure S4a, we reproduce the spatial variations in k_F of the Pd-derived bulk bands, illustrating a reduced k_F on a CrO_2 terminated surface as compared to the Pd-terminated areas. To allow for a direct comparison between the Pd-derived states probed on the two surface terminations, we plot the resulting peak positions from fits to the MDCs of the Pd-derived states shifted by their respective k_F (blue and yellow lines) in Figure S4b. The resulting Fermi velocity (v_F) of these states, fitted using a linear approximation, is plotted on top of the data (red and purple solid lines). For the CrO_2 -terminated surface we find a $v_F = 4.2 \pm 0.1 \text{ eV\AA}$ which is slightly smaller than for the Pd-terminated surface where $v_F = 4.6 \pm 0.1 \text{ eV\AA}$. The lowering of v_F for the CrO_2 -terminated surface is in agreement with our calculations which show a small charge transfer between the surface CrO_2



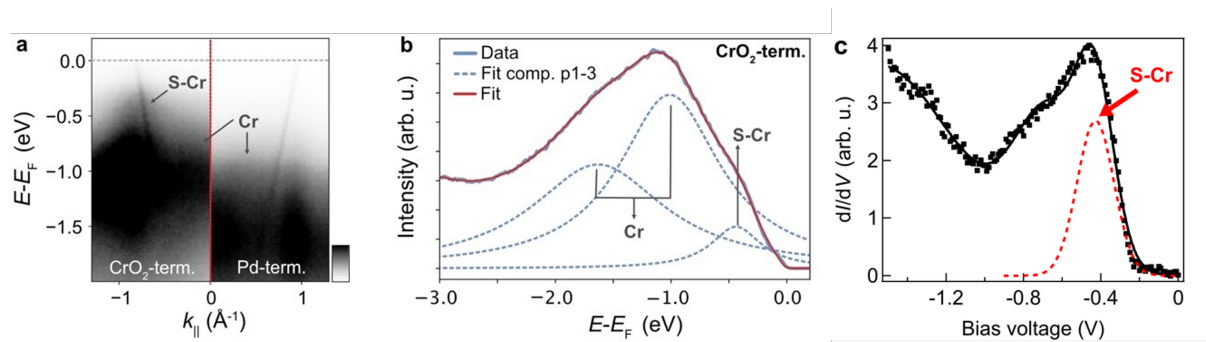
Supplementary Figure S4: **Termination-dependent variations of k_F .** (a) spatial map of the Fermi wave vector as shown in fig. 2c of the main text. (b) linear fits to the dispersion relation from which the Fermi wave vector has been extracted. Small but systematic deviations can be seen in the Fermi velocity.

and the subsurface Pd layer (Fig S13). Such a charge transfer indicates an enhanced coupling between the Pd and Cr-derived states. This can be expected to lead to a reduced k_F (slight hole-doping on the subsurface Pd layer) and reduced v_F (due to the increase in Cr character in these states) of the subsurface Pd states measured here. This is entirely consistent with our experimental findings shown in Figure S4.

Supplementary note 4. Comparison of tunneling spectra with photoemission

In fig. S5, we show additional data highlighting the differences in photoemission between Pd- and CrO_2 -terminated patches, as well as a detailed comparison between photoemission and tunneling spectroscopy. From the photoemission data (fig. S5a), we observe in the data of the CrO_2 terminated surface clear development of a low-energy shoulder at a binding energy of approximately -0.5eV (S-Cr), which is completely absent in the data of the Pd terminated surface. This S-Cr shoulder is also evident in the momentum-integrated data in fig. S5b, where it shows up as a change in the slope of the curve in the vicinity of the Fermi level, and can be clearly resolved in peak fits to the data. Specifically, through peak fitting to the EDC using

one component for the S-Cr shoulder and other components for peaks at higher binding energy we determined the binding energy of the S-Cr peak to be approximately -0.44eV . This value is in good agreement with the peak observed in our differential conductance spectra recorded with STM. In fig. S5(c), we show a fit to the peak at the gap edge in the tunneling spectrum, and determine an energy of -0.43eV , very close to the energy of the S-Cr component found in photoemission. We conclude that in both STM and ARPES we have observed independent evidence for the surface gap of the CrO_2 termination.

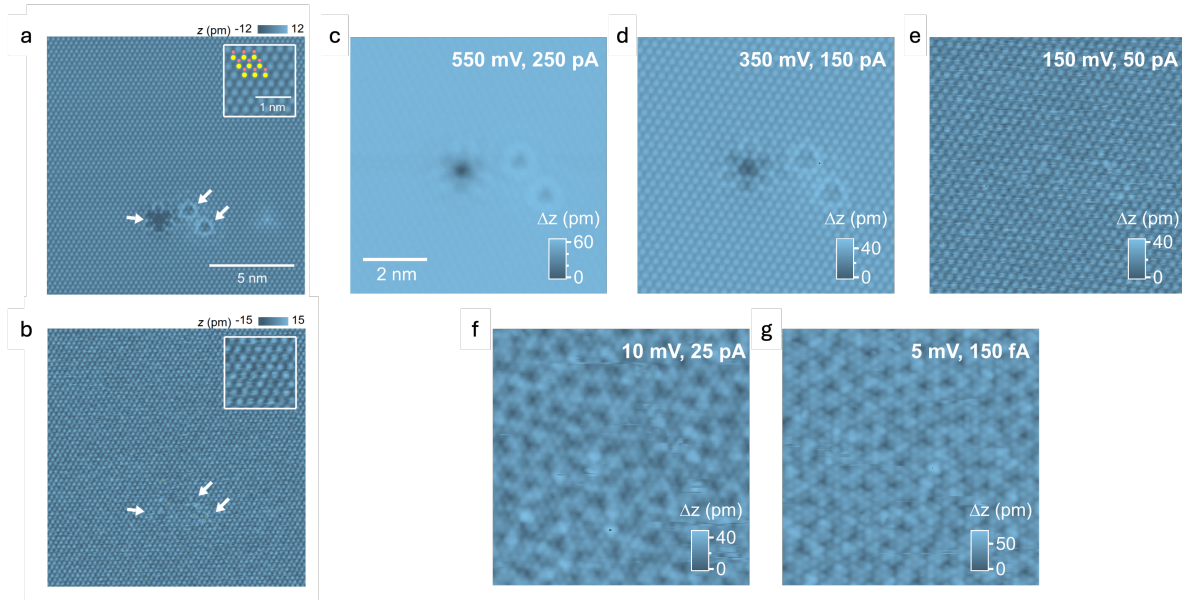


Supplementary Figure S5: **Comparison of tunneling spectra and photoemission.** **a** High resolution ARPES data of a CrO_2 - (left) and Pd-terminated (right) area of the sample. Both spectra have been probed using a photon energy of 110eV and LH polarised light. **b** The k -integrated spectra of the CrO_2 -terminated data extracted from a. By fitting the data, a clear multi-peak structure is revealed (see fit components 1-3, blue dashed lines) which is attributed to the presence of the bulk components of the Cr-derived states (labelled Cr) as well as the formation of a surface component (S-Cr), which results in the observed shoulder in the k -integrated data. **c** STS data (black dots) of the CrO_2 terminated surface of the sample taken within the sample bias range between -1.5V and $+1.5\text{V}$. ($V_s = 1.5\text{V}$, $I_s = 50\text{pA}$, $V_{\text{mod}} = 10\text{mV}$). Only data points for negative bias voltages, i.e. in the occupied states, are shown. Black line: numerical fit to the STS data. Red dotted line: peak associated with the Cr-derived surface states ($E = -0.43\text{eV}$).

Supplementary note 5. Bias-dependence of STM imaging and spectroscopy of charge order

We have imaged the CrO_2 -terminated surface of PdCrO_2 at energies both outside ($V = 350\text{mV}$) and inside the gap ($V = 150\text{mV}$). Shown in Fig. S6, the point defects in the CrO_2 surface layer are clearly visible at $V = 350\text{mV}$; however, they become virtually invisible when

imaged at energies inside the energy gap.

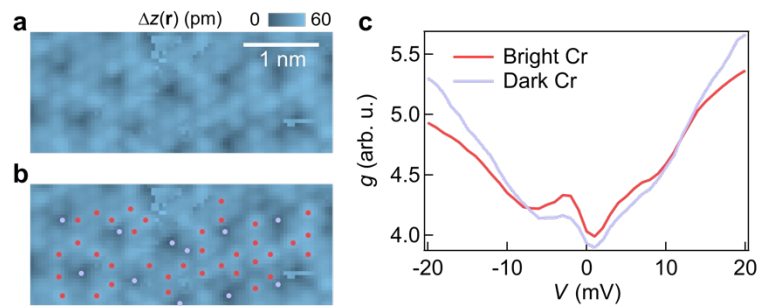


Supplementary Figure S6: **Bias voltage dependence of the appearance of point defects in the CrO₂ terminated surface.** Atomically resolved STM topographs of the CrO₂-terminated surface taken at scan parameters of (a) $V = 350\text{mV}, I = 150\text{pA}$ and (b) $V = 150\text{mV}, I = 50\text{pA}$ respectively. Image size: $(30\text{nm})^2$. The images show the point defects (indicated by white arrows) become virtually invisible when imaged at bias voltages V inside the gap. **c-e**, Images taken at the same surface location at different sample biases and tunneling currents (V, I): (c) $550\text{mV}, 250\text{pA}$, (d) $350\text{mV}, 105\text{pA}$, (e) $150\text{mV}, 50\text{pA}$. Image size: $(8\text{nm})^2$. As in a and b, the surface point defects showing up in the high sample bias images (c and d) become barely visible in the image taken at 150mV (e). Images taken in this bias range ($150 - 550\text{mV}$) show perfect triangular lattice of the CrO₂ surface. **f, g**, Images taken at energies in the vicinity of the Fermi level. Image size: $(8\text{nm})^2$. The image in (f) was recorded at $V = 10\text{mV}, I = 25\text{pA}$, while that in (g) was taken with much lower tunneling current ($V = 5\text{mV}, I = 150\text{fA}$). Note that the images in (f) and (g) were recorded using different frame angles. Both images show the glassy structure. However, due to the much lower current used, the image in (g) shows much fewer streaks.

The unusual changes in the appearance of topographic images with bias voltage V and current I are further highlighted in fig. S6c-g. The images taken in the sample bias range between 150mV and 550mV (fig. S6c-e) show a perfect triangular lattice with no evidence of the order however some evidence of fluctuations, e.g. in panel e where some streaky appearance can be seen. The image contrast becomes drastically different when the sample bias is decreased to

values of only a few millivolts and small currents. As shown in fig. S6f, g, the images taken at 10mV or below exhibit the short-range ordered glassy structure instead of the perfect triangular structure. In addition, at roughly fixed sample bias (5 – 10mV), when lowering the current by ~ 150 times (25pA \rightarrow 0.15pA), the streaks occasionally present in (f) become much less frequent in appearance in (g). All these images indicate that the perfect triangular lattice of the CrO₂ surface shows up when the surface is imaged at energies outside the surface gap and the glassy structure dominates when imaged at energies inside the gap. In addition, in order to image the glassy structure without any tip-induced disruption to the structure, imaging of the surface needs to be performed at very low sample bias (a few mVs) and extremely low tunnelling currents (~ 200 fA). This at the same time indicates that the characteristic energy scale associated with any excitations taking place in the glassy structure is in the few milli-electronvolt range.

In Fig. S7, we show tunneling spectra obtained on bright and dark atoms on the CrO₂ surface. There are clear differences in the shoulders around $+/- 5$ meV.



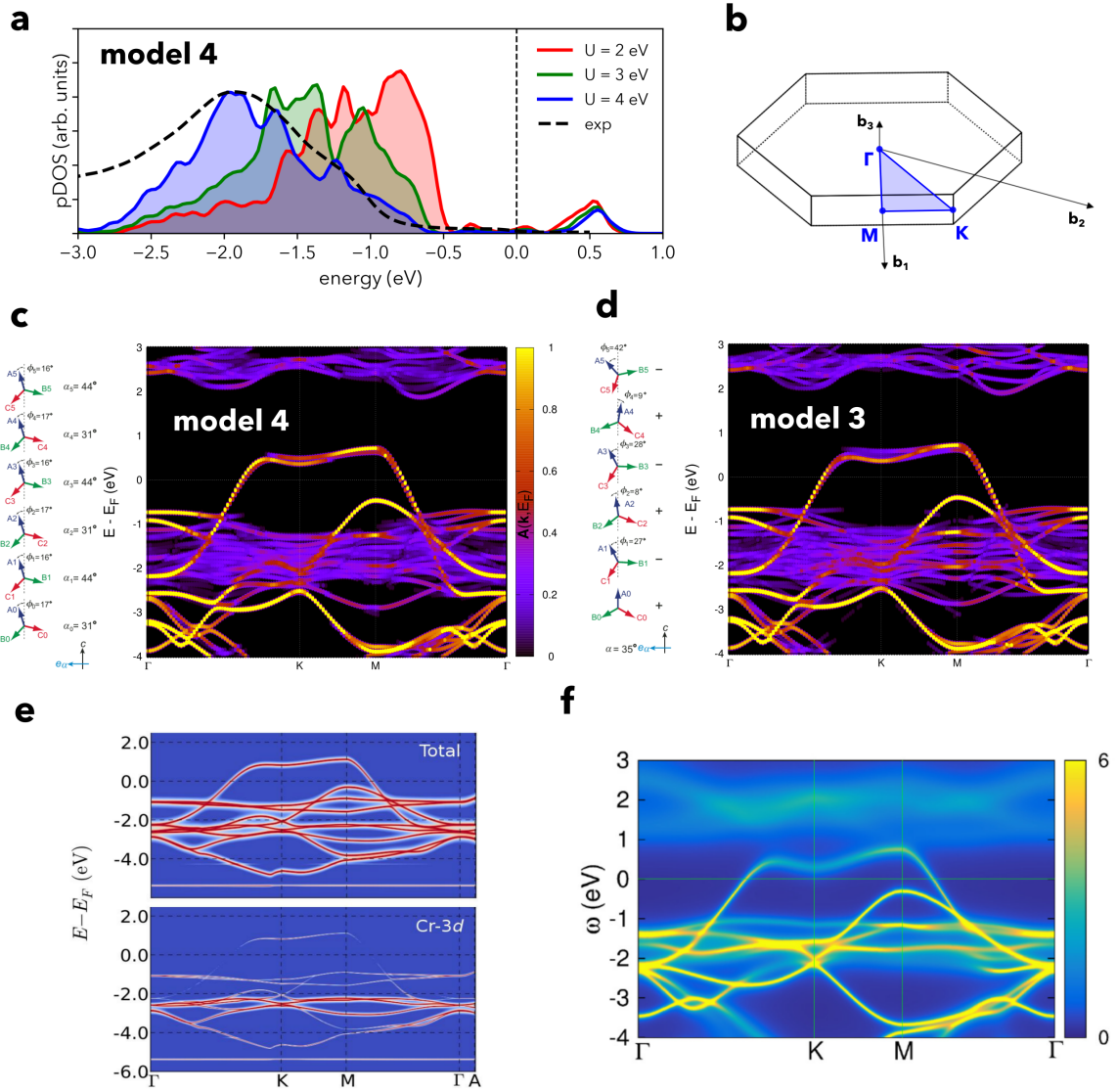
Supplementary Figure S7: **Tunnelling spectroscopy on the CrO₂ terminated surface.** a, atomically resolved STM topographic image taken from the CrO₂-terminated surface of PdCrO₂ ($V = 20$ mV, $I = 30$ pA, Size = 4×1.5 nm²). b, As (a), with overlaid dots of different colours marking the positions of the 'bright' (red) and 'dark' (light blue) Cr ions at which point differential conductance spectra $g(V)$ were taken. c, Averaged $g(V)$ spectra taken from the 'bright' (red) and 'dark' (light blue) Cr atoms. Spectroscopy setpoint $V_s = 20$ mV, $I_s = 100$ pA. Frequency and amplitude of bias modulation used $f_m = 413$ Hz, $V_m = 1$ mV.

Supplementary note 6. Calibration of the DFT+ U computational approach

Due to the correlated nature of the electronic states in the delafossite PdCrO_2 , their realistic modelling requires corrections that account for these correlations beyond conventional DFT. Here, we include these by undertaking calculations in the DFT+ U approach. We have performed extensive tests of the DFT+ U approach and compared the results both to experimental data and to calculations using DFT+DMFT to verify the fidelity in describing the correlated band structure. We have modelled bulk PdCrO_2 by using a $\sqrt{3} \times \sqrt{3}$ supercell with 6 layers, as described in the Methods section of the main text. We have performed calculations accounting for the noncollinear spin configuration of the antiferromagnetic (AF) noncoplanar 120° spin configuration (model 4 in ref.⁵) depicted in Fig. S8c. For different Hubbard values $U = 2, 3, 4$ eV and fixed Hund's coupling $J = 0.9$ eV, we have performed self-consistent field calculations and projected the density of states onto the Cr d orbitals (PDOS). The PDOS obtained from DFT+ U calculations is compared to the PDOS extracted from resonant photoemission measurements (Fig. 2c of Ref.⁶). As evident from Fig. S8a, $U = 4$ eV and $J = 0.9$ eV yield the best agreement between the DFT-calculated and measured PDOS. Therefore, we used these values in all our DFT+ U calculations.

To inspect how the particular AF spin configuration influences the electronic structure, we calculated the band structure of the "model 4" and "model 3" spin configurations from Ref.⁵. The total energies of the two configurations obtained from DFT+ U are very similar, with "model 4" being only 0.7 meV per Cr atom lower in energy compared to "model 3". These spin configurations differ in relative orientation of the 120° spin planes in subsequent CrO_2 layers. The band structures corresponding to two spin configurations are unfolded to the Brillouin zone of the primitive cell (Fig. S8b) and depicted in Fig. S8c and d, with the corresponding spin configurations displayed on the left of each panel. As these band plots are very similar in a wide energy range, we conclude that the magnetic coupling between adjacent CrO_2 layers has only a minor effect on the overall electronic structure of the system.

Compared to the electronic structure calculated with DMFT⁶⁻⁸, the DFT+ U approach with $U = 4$ eV is performing quite well. By comparing the Pd-derived bands from Fig. S8c with the DMFT calculations shown in Fig. S8e and f, the single dispersive band crossing E_F is very

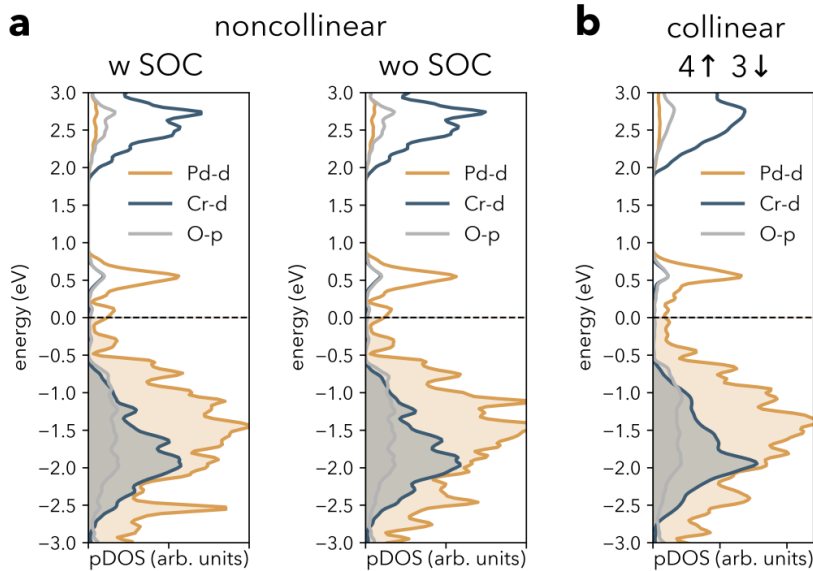


Supplementary Figure S8: **Bulk electronic structure of PdCrO₂**. (a) Projected density of states (PDOS) of Cr 3d orbitals obtained from DFT+ U calculations, including relativistic corrections and noncollinear spin order, for different U and $J = 0.9$ eV, compared to the PDOS extracted from the photoemission measurements in Ref.⁶ (black dashed line). (b) Brillouin zone of the primitive cell. (c, d) Effective band structures, unfolded to the Brillouin zone of the primitive cell, for the "model 4" and "model 3" spin configurations taken from Ref.⁵. Panels to the left depict the spin configurations (adapted from Fig. 5 of Ref.⁵). The band structure from DMFT calculations is shown in panels e⁶ and f⁷ for comparison. Models in panel c, d reprinted with permission from Ref.⁵, Copyright (2014) by the American Physical Society.

similar in the two approaches, and so is the band reaching its maximum at the M point just be-

low E_F . The band splitting observable in the DFT+ U band structure at Γ slightly above -1 eV (Fig. S8c) is due to spin-orbit coupling (SOC). We expect that this splitting is not observable in Fig. S8e and f since SOC was not included in the DMFT calculations. Concerning the Cr-derived bands, DMFT shows them lying in the range from -2.5 eV to -1 eV. This agrees with our DFT+ U band structure for $U = 4$ eV. The choice of U is crucial for the position of these bands, with higher U values shifting them towards higher binding energies.

With U fixed at 4 eV, we performed the calculations on bulk PdCrO₂ in three different ways: (1) by using the $\sqrt{3} \times \sqrt{3}$ unit cell and the "model 4" AF-120 spin configuration within the non-collinear DFT+ U approach and including spin-orbit coupling, (2) using the same AF-120 spin configuration within non-collinear DFT+ U but without spin-orbit coupling and (3) by using the $\sqrt{7} \times \sqrt{7}$ unit cell and the "4-up 3-down" collinear spin configuration within the spin polarised DFT+ U approach (see Methods section of the main text). The PDOS plots obtained from the two approaches are displayed in Fig. S9. Firstly, from Fig. S9a, we conclude that



Supplementary Figure S9: **PDOS of bulk PdCrO₂ from three different approaches.** (a) PDOS of noncollinear "model 4" AF-120 spin configuration calculated using the $\sqrt{3} \times \sqrt{3}$ unit cell with spin-orbit coupling (SOC) (left) and without SOC (right). (b) PDOS calculated within spin-polarised DFT+ U approach using the $\sqrt{7} \times \sqrt{7}$ unit cell with four layers, with 4 and 3 opposite spins in collinear configuration distributed among the layers in an alternating way as described in the Methods section of the main text.

SOC plays a minor role in the electronic structure of PdCrO₂, especially for the Cr-derived states. Secondly, the PDOS obtained from collinear calculations, Fig. S9b, looks very similar to that from noncollinear calculations, with very similar band widths in the two cases and major resonances showing up at the same energies. Therefore, we conclude that for treating of the CrO₂ surface we can neglect SOC and turn to the computationally much more affordable spin-polarised DFT calculations.

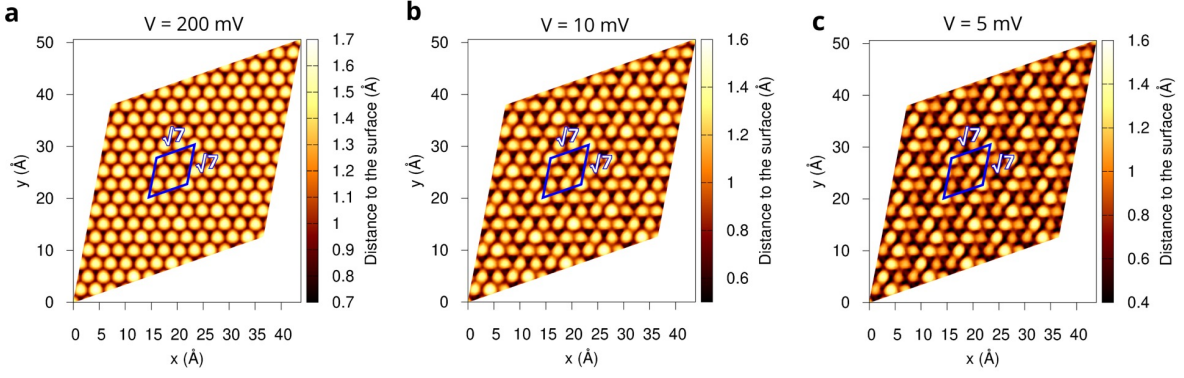
Supplementary note 7. Simulated STM images of the CrO₂ surface

For comparison, we provide in Fig. S10 simulated STM images which show that indeed the reconstructed CrO₂ surface reveals patterns that look similar to the experimentally observed ones obtained at very low bias voltages. We note that in experiment, the surface structure cannot be imaged with bias voltages $|V| > 20\text{mV}$, because the tunneling electrons induce changes in the order in the surface layer.

By changing the bias voltage in DFT simulations, we are able to capture the most prominent features of experimental STM images: at larger bias voltages ($V = 200\text{mV}$, Fig. S10a) a perfect triangular lattice can be observed, with no evidence of the $\sqrt{7} \times \sqrt{7}$ reconstruction. On the other hand, at small bias voltages, when only the Pd-derived electronic states close to the Fermi energy and located inside the surface gap are probed (Fig. S10b,c), we clearly observe a difference in contrast due to the two types of Cr atoms, with a spatial variation that is consistent with the local contrast observed in our measurements. We note that the contrast variation is more inhomogeneous in our experiments, however, consistent with the glassy nature of this state. Note that the STM images do not capture the Cr states directly (these states are gapped away) but instead the subsurface Pd states by tunnelling through the CrO₂ layer.

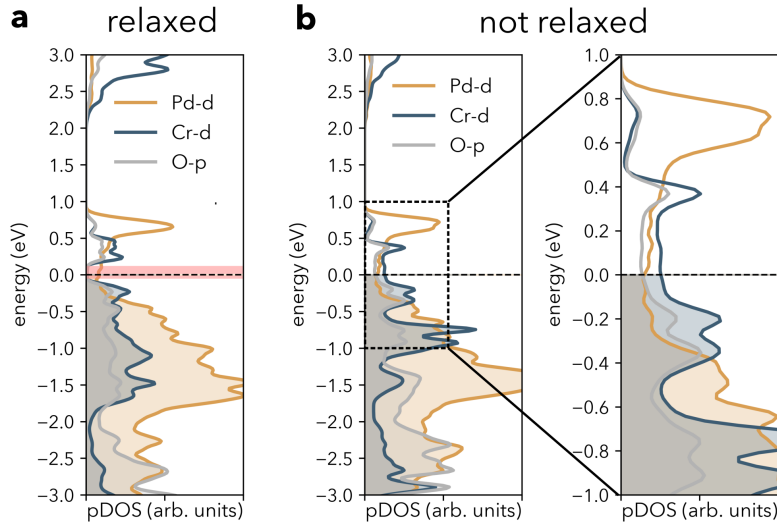
Supplementary note 8. Influence of the atomic relaxation and spin configuration on the band gap in surface CrO₂ layer

In the main text we concluded that the surface relaxation is necessary for the band gap opening in the CrO₂ layer. To demonstrate this we performed additional calculations for the unrelaxed surface, assuming bulk-like atomic positions of Cr atoms and the FM spin configura-

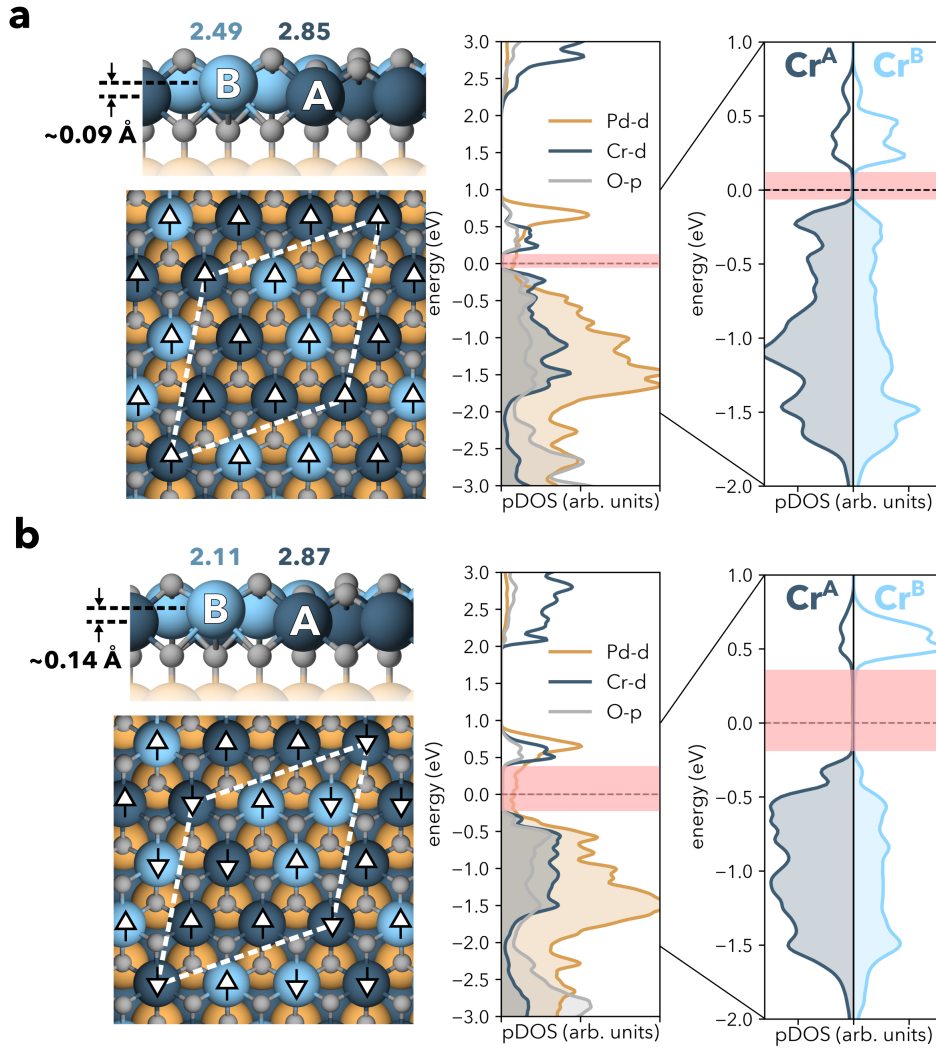


Supplementary Figure S10: **Simulated STM images.** Simulated STM images obtained in constant-current mode at (a) $V = 200$ mV, showing a perfectly triangular lattice, and (b, c) at 10 mV and 5 mV, respectively, showing the $\sqrt{7} \times \sqrt{7}$ reconstruction.

tion. The PDOS plots in Fig. S11b clearly show the metallic surface, with Cr $3d$ states giving a dominant contribution in the whole energy interval from -0.4 to 0.4 eV around E_F . As the Cr atoms from the unrelaxed surface are symmetry-equivalent, there is no mechanism that would allow their division into two distinct types and the charge disproportionation does not occur.



Supplementary Figure S11: **Effect of surface relaxation on the gap opening.** (a) PDOS for relaxed surface. (b) PDOS for unrelaxed surface with ferromagnetic order, including a zoom-in onto the energy range around the Fermi energy. No band gap is observed. The band gap opens only after the surface is relaxed. Surface relaxation, starting from positions inherited from the bulk, lowers the total energy by 160 meV/Cr.



Supplementary Figure S12: **Spin configuration at the surface and its relation to the size of the gap.**

(a) Ferromagnetic configuration from the main text and (b) the "4-up 3-down" configuration. The type of Cr atoms is not related to the magnetic moment direction, i.e. there are both spin-up and spin-down Cr^A (Cr^B) atoms.

The surface spin configuration, although not responsible for the band gap opening, can affect its size. To shed light on its influence, we performed surface relaxations with a $\sqrt{7} \times \sqrt{7}$ unit cell starting from a spin configuration with 4 spin-up and 3 spin-down Cr atoms that we refer to as "4-up 3-down" spin configuration (Fig. S12). After the relaxation, the structure ended in a local minimum that is 2.6 meV/Cr higher in energy than the ferromagnetic surface but which has some features, apart from the magnetic order, clearly distinguishing this metastable state from the ferromagnetic ground state. Firstly, the band gap is much larger (~ 0.6 eV) compared

to the ferromagnetic surface (~ 0.2 eV). This is a joint effect of the absence of FM exchange in the "4-up 3-down" state and of the more pronounced surface reconstruction, as evidenced by larger displacement of Cr^B atoms as compared to the FM state (Fig. S12b, left panel). It is worth noting that in the "4-up 3-down" configuration the projection of the magnetic moment is *not* related to the type of Cr atom, i.e. there are both spin-up and spin-down magnetic moments among both Cr types. However, the magnitude of the magnetic moment is tied to the Cr type, with Cr^A (Cr^B) always having the magnetic moments with magnitude of 2.87 (2.11) μ_B .

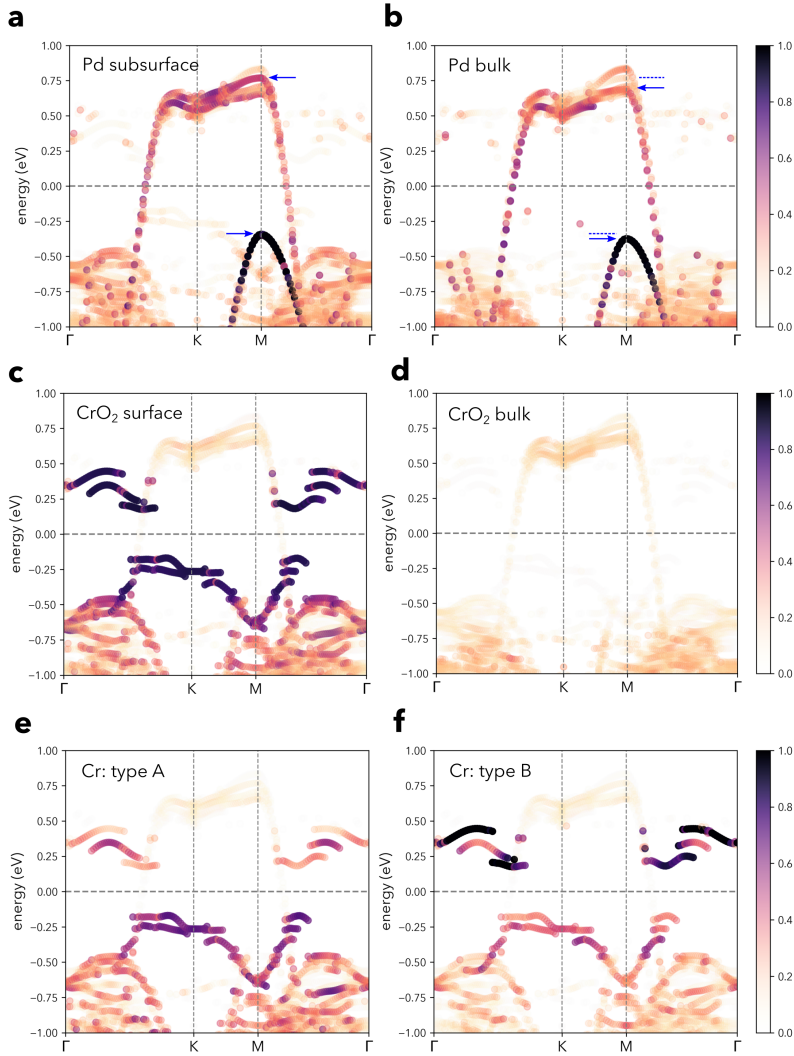
Supplementary note 9. Layer-resolved electronic band structure

To analyze charge transfer to the Pd-layers, we have determined the band structure from spin-polarised DFT+*U* calculations in the $\sqrt{7} \times \sqrt{7}$ unit cell, unfolded them to the primitive cell (Brillouin zone shown in Fig. S8b) and projected onto the different layers. The Pd-derived band crossing the Fermi energy E_F in the bulk is in the topmost Pd layer moved by ~ 0.1 eV towards lower binding energies as compared to the bulk (Fig. S13a, b). The same shift can be observed for the band maximum at the *M* point. This band shift suggests that the subsurface Pd layer is hole doped compared to the bulk.

For completeness, we show the CrO₂-bands, with contributions from Cr and O atoms summed up. We can clearly see that in the energy range from -1 eV to 1 eV there is only the contribution from the surface layer, as the bulk CrO₂ bands are at higher binding energies (Fig. S13c, d). We further projected the band structure of the CrO₂ surface on two types of Cr atoms. Evidently, Cr^A (Cr^B) atoms contribute more than Cr^B (Cr^A) atoms in the energy window below (above) the E_F , which is consistent with the PDOS plot of Fig. 3c of the main text showing that Cr^B atoms are more strongly hole doped.

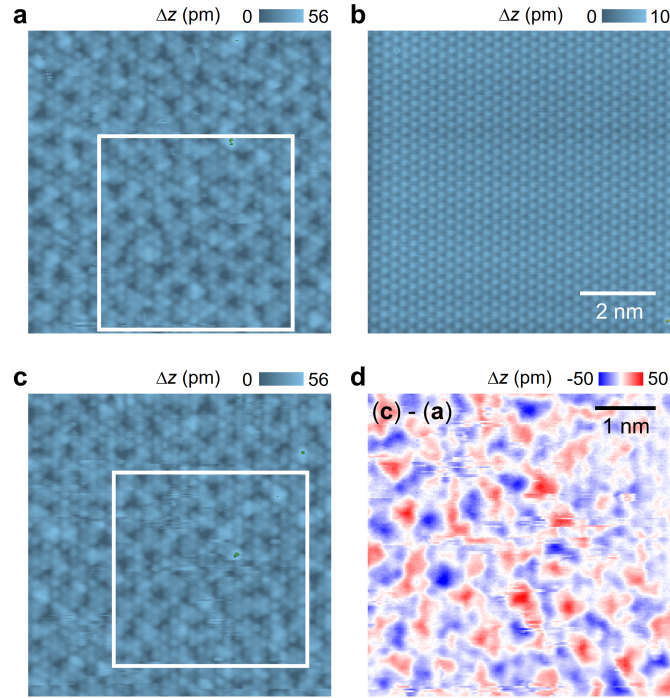
Supplementary note 10. Imaging of the charge-disproportionated order

To demonstrate the sensitivity of the charge-ordered insulating state to the tunneling conditions chosen, we first imaged the order at $V = 5$ mV, then at a higher bias voltage of 200 mV, and then at $V = 5$ mV again. The obtained images are shown in Fig. S14, a to c. To demonstrate



Supplementary Figure S13: **Layer-resolved band structure** (a) Band structure of the subsurface Pd layer and (b) of the subsequent Pd layer below it, that we refer to as the bulk Pd layer. (c) Band structure of the surface and (d) the bulk CrO₂ layer. The band structure of the surface CrO₂ layer is further projected onto two types of Cr atoms in (e) and (f).

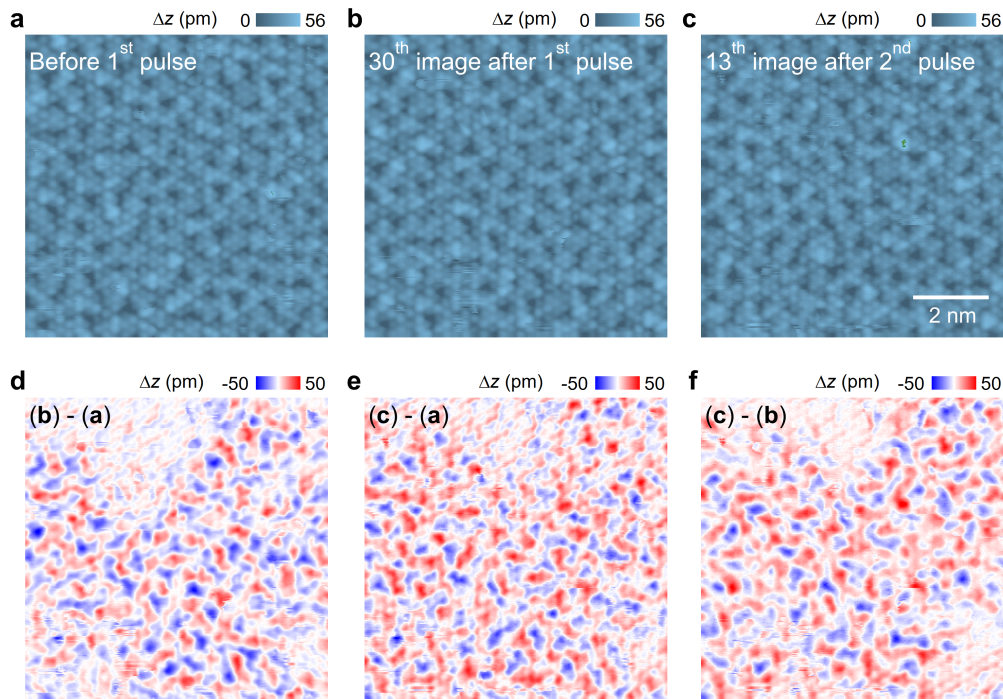
any change in the ground-state spin order caused by the scan with $V = 200\text{mV}$ (Fig. S14b), in Fig. S14d we show the difference image formed by subtraction of the cropped region in Fig. S14c by that in Fig. S14a. The difference image shows drastic change in the charge order after the scan with $V = 200\text{mV}$.



Supplementary Figure S14: **Bias-voltage induced change in the charge order.** **a**, STM topographic image of the CrO_2 terminated surface recorded at low bias voltage $V = 5\text{mV}$. **b**, Image taken at higher voltage $V = 200\text{mV}$ after **(a)**. **c**, low voltage image ($V = 5\text{mV}$) taken after **(b)**. Image size: $(8\text{nm})^2$. Scan parameters: **(a,c)** $V = 5\text{mV}$, $I = 150\text{fA}$; **(b)** $V = 200\text{mV}$, $I = 10\text{pA}$. **d**, Difference image obtained by subtraction of the cropped region (marked by a square) in the image in **(c)** from that in **(a)**.

Supplementary note 11. Pulse-induced change in the charge order

To investigate if the charge order evolves back to the original ground state configuration after excitation, we performed two sets of experiments. In the first experiment, we continuously imaged the order using very mild scanning parameters, ($V = 5\text{mV}$, $I = 150\text{fA}$), and amid imaging we occasionally applied voltage pulses ($V = 70\text{mV}$, $\Delta t = 2\text{s}$) to trigger changes in the charge order, and monitored its relaxation. To show our experimental results, in Fig. S15, a to c, we show the image taken before the application of any voltage pulse (Fig. S15a), that taken 312 minutes after the application of the first voltage pulse (Fig. S15b), and that recorded 129 minutes after the application of the second voltage pulse (Fig. S15c). The images look very different from each other. To visualize the changes, we also show their difference images in Fig. S15, d to f, showing drastic changes in the order caused by the voltage pulse(s).



Supplementary Figure S15: **Pulse induced change in the short-range order.** **a**, Atomically resolved STM image of the CrO₂ terminated surface, taken before application of any voltage pulse ($V = 70\text{mV}$, $\Delta t = 2\text{s}$) to the centre of the imaged region. **b**, The 30th image recorded 312 minutes after application of the first voltage pulse. **c**, The 13th image recorded 129 minutes after application of the second voltage pulse. Image size: $(8\text{nm})^2$. Scan parameters: $V = 5\text{mV}$, $I = 150\text{fA}$. All images were recorded at the exact same surface location, under extremely stable, drift-free tunneling condition. **d-f**, Difference images obtained by subtraction between different image pairs formed between (a), (b) and (c) respectively.

References

1. Chi Ming Yim, Dibyashree Chakraborti, Luke C. Rhodes, Seunghyun Khim, Andrew P. Mackenzie, and Peter Wahl. Quasiparticle interference and quantum confinement in a correlated Rashba spin-split 2D electron liquid. *Sci. Adv.*, 7(15):eabd7361, April 2021.
2. Veronika Sunko, H. Rosner, P. Kushwaha, S. Khim, F. Mazzola, L. Bawden, O. J. Clark, J. M. Riley, D. Kasinathan, M. W. Haverkort, T. K. Kim, M. Hoesch, J. Fujii, I. Vobornik, A. P. Mackenzie, and P. D. C. King. Maximal Rashba-like spin splitting via kinetic-energy-coupled inversion-symmetry breaking. *Nature*, 549(7673):492–496, 2017.

3. Federico Mazzola, Veronika Sunko, Seunghyun Khim, Helge Rosner, Pallavi Kushwaha, Oliver J. Clark, Lewis Bawden, Igor Marković, Timur K. Kim, Moritz Hoesch, Andrew P. Mackenzie, and Phil D. C. King. Itinerant ferromagnetism of the Pd-terminated polar surface of PdCoO₂. PNAS, 115(51):12956–12960, December 2018.
4. F. Mazzola, C. M. Yim, V. Sunko, S. Khim, P. Kushwaha, O. J. Clark, L. Bawden, I. Marković, D. Chakraborti, T. K. Kim, M. Hoesch, A. P. Mackenzie, P. Wahl, and P. D. C. King. Tuneable electron–magnon coupling of ferromagnetic surface states in PdCoO₂. npj Quantum Materials, 7(1):20, 2022.
5. Hiroshi Takatsu, Gwilherm Nénert, Hiroaki Kadowaki, Hideki Yoshizawa, Mechthild Enderle, Shingo Yonezawa, Yoshiteru Maeno, Jungeun Kim, Naruki Tsuji, Masaki Takata, Yang Zhao, Mark Green, and Collin Broholm. Magnetic structure of the conductive triangular-lattice antiferromagnet PdCrO₂. Phys. Rev. B, 89:104408, Mar 2014.
6. V. Sunko, F. Mazzola, S. Kitamura, S. Khim, P. Kushwaha, O. J. Clark, M. D. Watson, I. Marković, D. Biswas, L. Pourovskii, T. K. Kim, T.-L. Lee, P. K. Thakur, H. Rosner, A. Georges, R. Moessner, T. Oka, A. P. Mackenzie, and P. D. C. King. Probing spin correlations using angle-resolved photoemission in a coupled metallic/Mott insulator system. Sci. Adv., 6(6):eaaz0611, February 2020. Figures reproduced under CC-BY license.
7. Frank Lechermann. Hidden Mott insulator in metallic PdCrO₂. Phys. Rev. Materials, 2(8):085004, August 2018.
8. Frank Lechermann. From basic properties to the Mott design of correlated delafossites. npj Comput. Mater., 7(120):1–17, July 2021.